Supplementary Information

Methods

Raw materials

All the powder samples were synthesized using $RuCl_3 \cdot nH_2O$ (99.98%, Sigma-Aldrich), $Mg(NO_3)_2 \cdot 6H_2O$ (99%, Sigma-Aldrich), $AlCl_3 \cdot 6H_2O$ (99%, Sigma-Aldrich), $Ca(NO_3)_2 \cdot 4H_2O$ (99.98%, Sigma-Aldrich), $ScCl_3 \cdot nH_2O$ (99.9%, Sigma-Aldrich), $Ti[OCH(CH_3)_2]_4$ (99.999%, Sigma-Aldrich, for sol–gel synthesis), $TiCl_3$ solution (10–15%, Sigma-Aldrich, for hydrothermal synthesis), VCl_3 (99%, Alfa Aesar), $Cr(NO_3)_3 \cdot 9H_2O$ (99.99%, Sigma-Aldrich), $MnCl_2 \cdot 4H_2O$ (99.99%, Sigma-Aldrich), $Fe(NO_3)_3 \cdot 9H_2O$ (≥99.95%, Sigma-Aldrich), $Co(NO_3)_2 \cdot 6H_2O$ (99.999%, Alfa Aesar), $NiCl_2 \cdot 6H_2O$ (99.9%, Sigma-Aldrich), $Cu(NO_3)_2 \cdot 2.5H_2O$ (99.99%, Sigma-Aldrich), $Zn(NO_3)_2 \cdot 6H_2O$ (99.998%, Alfa Aesar), $Ga(NO_3)_3 \cdot nH_2O$ (99.9%, Sigma-Aldrich), GeO_2 (99.999%, Sigma-Aldrich, for sol–gel synthesis), $SrCl_2 \cdot 6H_2O$ (≥99.995%, Sigma-Aldrich), $ZrOCl_2 \cdot nH_2O$ (99.99%, Sigma-Aldrich), $C_4H_4NNbO_9 \cdot nH_2O$ (99.99%, Sigma-Aldrich), $(NH_4)_6Mo_7O_{24} \cdot 4H_2O$ (99%, Sigma-Aldrich), $In(NO_3)_3 \cdot nH_2O$ (99.99%, Sigma-Aldrich), $SnCl_4 \cdot 5H_2O$ (98%, Sigma-Aldrich), $SbCl_3$ (99.95%, Sigma-Aldrich), $BaCl_2 \cdot 2H_2O$ (≥99%, Sigma-Aldrich), $La(NO_3)_3 \cdot 6H_2O$ (99.99%, Sigma-Aldrich), $Ce(NO_3)_3 \cdot 6H_2O$ (99.999%, Sigma-Aldrich), $Pr(NO_3)_3 \cdot 6H_2O$ (99.9%, Sigma-Aldrich), $Nd(NO_3)_3 \cdot 6H_2O$ (99.9%, Sigma-Aldrich), $HfOCl_2 \cdot nH_2O$ (99.99%, Sigma-Aldrich), $Ta(OC_2H_5)_5$ (99.98%, Sigma-Aldrich), $(NH_4)_6H_2W_{12}O_{40} \cdot nH_2O$ (99.99%, Sigma-Aldrich), and $IrCl_3 \cdot 3H_2O$ (Acros Organics) as starting materials. The solvents and chemical reagents used in the powder synthesis included ethylene glycol (99.8%, Sigma-Aldrich), nitric acid (60.0%, Samchun), hydrogen peroxide solution (30% in H_2O, Sigma-Aldrich), NaOH (99.99%, Sigma-Aldrich), citric acid (≥99.5%, Sigma-Aldrich), D-(+)-glucose (≥99.5%, Sigma-Aldrich), and urea (≥98%, Sigma-Aldrich).

Syntheses of polycrystals

To obtain polycrystals larger than 100 nm, a sol–gel-based Pechini method was used at temperatures ranging from 700 to 850°C. A precursor solution was prepared by dissolving 0.4 mmol of $RuCl_3 \cdot nH_2O$, 0.1 mmol of the foreign metal precursor, and 0.5 mmol of citric acid in 100 mL of deionized water (Milli-Q water). For the preparation of Ti and Ta precursors, 20 mM of stock solutions were prepared in ethanol with citric acid in an equimolar ratio to the metal ions inside a glove box to prevent unwanted hydrolysis. The solution was continuously stirred and heated at 70°C for 1 h to ensure complete dissolution, followed by the addition of 1.5 mmol of ethylene glycol. The solvent was then evaporated at 150°C. The resulting gel was finely ground and subjected to further annealing to obtain the final powders. For the synthesis of pristine RuO_2, the same procedure was adopted, using 0.5 mmol of $RuCl_3 \cdot nH_2O$ without the addition of a foreign precursor. The annealing conditions varied depending on the element: samples with Al, Sc, Ga, Ge, Nb, Ba, and Nd were annealed at 800°C for 48 h; the V sample at 800°C for 24 h; the Ti sample at 800°C for 60 h; and the Ta sample at 850°C for 48 h. All other samples were annealed at 700°C for 10 h.

Both sol–gel and hydrothermal methods were utilized to acquire solid-solution RuO_2 nanocrystals smaller than 20 nm. For the synthesis of solid-solution samples with Ti, Cr, Fe, Co, Ni, Cu, Zr, and Hf, a hydrothermal method was used. Aqueous solutions containing 0.4 mmol of $RuCl_3 \cdot nH_2O$ and 0.1 mmol of each foreign metal precursor were prepared in deionized water. To suppress the formation of metallic species, 0.378 mL of hydrogen peroxide solution was added dropwise to each. To adjust pH, 1 M NaOH aqueous solution was introduced in varying amounts depending on the element: 7.56 mL of 1 M NaOH for samples with Co, Ni, and Cu; and 2.6 mL for samples with Zr and Hf. The total volume was adjusted to 45 mL with deionized water. The fully dissolved solutions were transferred to a PTFE-lined autoclave and annealed at 180°C for 1.5 h. After the reaction, the resulting products were washed several times with deionized water and ethanol, dried, and finally annealed to achieve

crystallinity. The annealing conditions were set to 300°C for 3 h for the pristine and Ni samples, while all other samples were annealed at 350°C for 3 h.

For solid-solution samples with Mg, Nb, Mo, and Ta, aqueous solutions were first prepared by dissolving 0.4 mmol of $RuCl_3 \cdot nH_2O$, 0.1 mmol of each foreign metal precursor, and 0.5 mmol of citric acid in 100 mL of deionized water. A stock solution of the Ta precursor in ethanol was used. The solutions were continuously stirred and heated at 70°C for 1 h. Then, 1.5 mmol of ethylene glycol and 1.5 mmol of nitric acid were added. Heating the mixtures to 150°C allowed for complete evaporation of the solvent, resulting to the formation of gels. The gels were ground into fine powders and subjected to annealing. Gels with Mg, Nb, and Ta were annealed at 450°C for 3 h and the Mo-containing gel was annealed at 500°C for 3 h. To track the temperature-dependent phase evolution in samples with Nb and Ta via X-ray diffraction, the gels were prepared as described above without nitric acid and heat-treated from 400 to 800°C in 50°C intervals at a heating rate of 2°C/min. The samples were rapidly removed from the furnace at each temperature for quenching.

For the synthesis of a solid solution with In, 0.4 mmol of $RuCl_3 \cdot nH_2O$, 0.1 mmol of the In precursor, and 0.5 mmol of citric acid were dissolved in 100 mL of deionized water. 50 mmol of nitric acid was also added to the solution. The mixture was heated at 90°C for 6 h, followed by further heating at 170°C for 12 h. The resulting gel was finely ground and annealed at 400°C for 3 h. To acquire solid-solution RuO_2 with Sb, a solution was prepared by dissolving 0.16 mmol of $RuCl_3 \cdot nH_2O$ and 0.04 mmol of the Sb precursor in 100 mL of ethanol. Ethanol was chosen as the solvent instead of water to prevent the formation of SbOCl. The solution was continuously stirred at room temperature for 1 h and subsequently heated at 120°C for 12 h for solvent evaporation. The resulting material was ground and annealed at 400°C for 3 h. A similar sol–gel procedure was utilized for synthesizing solid-solution RuO_2 samples with Al, Sc, V, Mn, Sn, and Ir. Solutions were prepared by dissolving 0.16 mmol of $RuCl_3 \cdot nH_2O$ and 0.04 mmol of the foreign metal precursors in mixtures containing 5 g of D-(+)-glucose and 1 g of urea in 5 mL of deionized water. The solutions were stirred for 30 min, then heated in an oven at 140°C for 8 h. After grinding, the gels were annealed at 400°C for 6 h for samples with Al, Sc, V, Sn, and Ir, and at 500°C for 6 h for the Mn sample.

XRD and XAS analyses

The crystal structure and phase analysis of the synthesized powder were examined using a high-resolution powder X-ray diffractometer (SmartLab, RIGAKU) with Cu K_α radiation. The obtained XRD data were analyzed by comparing them with the powder diffraction reference files to identify and assess the presence of secondary phases. The average particle size of solid-solution RuO_2 was determined using the Halder-Wagner method.[S1] This method simultaneously evaluates crystallite size and lattice strain, attributing Bragg peak broadening to both factors.

XANES and EXAFS measurements were carried out for the foreign elements in addition to Ru at the 7D beamline of PLS-II at the Pohang Accelerator Laboratory. The X-ray photon energy was monochromatized by using a Si (111) double crystal. The XAS experiments were performed in a fluorescence-transmission geometry setup, where sample spectra were recorded in fluorescence mode, while the reference material's spectrum was simultaneously measured in transmission mode at room temperature. Calibration of the Ru *K*-edge XANES spectra was performed using Ru foil as a reference, with the edge energy set at 22,117 eV. The raw XAS data were processed using ATHENA software, with the Ru *K*-edge position determined via the first-derivative method. The EXAFS data were analyzed using ATHENA software within the IFEFFIT suite. To enhance the signal, k^3-weighted EXAFS spectra were generated and fitted over a k range of 3–13 $Å^{-1}$. Due to the relatively broad nature of the Ru *K*-edge in XAS, first derivative curves of the Ru *K*-edge spectra were compared to more accurately assess the valence state of Ru in the samples.

STEM and EDS

Each powder sample for STEM observation was ultrasonically dispersed in high-purity ethanol for 15 min, and several drops were placed onto a lacey-carbon-film Cu or Au grid, followed by drying for 20 min. Conventional bright-field (BF) TEM images were acquired using a transmission electron microscope (Tecnai F30, Thermo Fisher Scientific) to measure the average nanoparticle size. Atomic-column-resolved STEM images were obtained using a transmission electron microscope (Spectra Ultra, Thermo Fisher Scientific) in high-angle annular dark-field (HAADF) and BF modes at 200 kV with spherical aberration correction for the electron probe. The optimum size of the electron probe was ~1.4 Å with a convergence semiangle of 21.4 mrad. The collection semi-angles of the STEM detectors were set to 63–200 mrad for HAADF imaging and 0–25 mrad for BF imaging. The beam current was maintained at ~20 pA to minimize the electron beam damage to the specimen. Chemical composition analysis with EDS was performed using the Spectra Ultra at 200 kV with six integrated silicon-drift EDS detectors at a collection solid angle of 4.04 srad. EDS mapping was also performed using another transmission electron microscope (Talos F200X, Thermo Fisher Scientific) at 200 kV along with four integrated silicon-drift EDS detectors at a collection solid angle of 0.7 srad to visualize the overall composition. The following X-ray emission lines were selected for elemental mapping and subsequent quantification: Ru-L_α (2.6 keV), Nb-L_α (2.2 keV), Ta-L_α (8.1 keV), Mg-K_α (1.3 keV), Al-K_α (1.5 keV), Ca-K_α (3.7 keV), Sc-K_α (4.1 keV), Ti-K_α (4.5 keV), V-K_α (5.0 keV), Cr-K_α (5.4 keV), Mn-K_α (5.9 keV), Fe-K_α (6.4 keV), Co-K_α (6.9 keV), Ni-K_α (7.5 keV), Cu-K_α (8.0 keV), Zn-K_α (8.6 keV), Ga-K_α (9.3 keV), Ge-K_α (9.9 keV), Sr-K_α (14.2 keV), Zr-L_α (2.0 keV), Mo-L_α (2.3 keV), In-L_α (3.3 keV), Sn-L_α (3.4 keV), Sb-L_α (3.6 keV), Ba-L_α (4.5 keV), La-L_α (4.7 keV), Ce-L_α (4.8 keV), Pr-L_α (5.0 keV), Nd-L_α (5.2 keV), Hf-L_α (7.9 keV), and Ir-L_α (9.2 keV). The EDS maps were low-pass filtered using Thermo Fisher Scientific Velox software to reduce background noise. Particle size measurements were performed using STEM images and analyzed via Feret's method.[S2] For each particle in the images, the longest and shortest caliper lengths were measured, and their average was taken as the particle size.

Electrochemical measurements

Electrochemical measurements were conducted in 0.1 M $HClO_4$ (pH ~1) solutions, which were prepared by diluting 70% $HClO_4$ (99.999%, Sigma-Aldrich) with Milli-Q water (18.2 MΩ·cm). A Pt wire served as the counter electrode, and an Ag/AgCl (3 M NaCl) electrode was used as the reference electrode. The applied potential was converted to the reversible hydrogen electrode (RHE) scale using the following equation: $E_{RHE} = E_{Ag/AgCl} + (0.059 \times pH) + 0.21$. All the measurements were carried out using a Biologic SP-300 potentiostat.

The ink was prepared by mixing 9.9 mg of catalyst particles, 99 μL of K^+-exchanged 5-wt% Nafion dispersion solution (D-521, Chemours), 9.333 ml of high-purity ethyl alcohol, and 4.568 mL of deionized water. The 10 μL ink was drop-casted inside a 3 mm PTFE-ring set on a PTFE-treated Toray carbon paper. The loading amount of catalysts was adjusted to be 0.1 mg/cm^2 for accelerated durability tests (ADT) and chronoamperometry (CA) measurements. Electrodes were dried at 80°C in an oven for 2 h before measurements. As reasonably addressed in a previous study,[S3] measuring the effective surface area in gas evolving electrodes is of great significance. Although the blockage of active sites by gas bubbles cannot be completely avoided, the double-layer capacitance (C_{DL}) was measured to determine the electrochemical active surface area (ECSA) before all experiments. The measurements were performed in the non-faradaic potential range (1.0–1.1 V_{RHE}) at scan rates of 150, 100, 75, 50, 25, and 10 mV/s without stirring. The C_{dl} was converted to ECSA using the equation: $ECSA = C_{DL}/C_s$, where C_s represents the C_s is the specific capacitance of the sample per unit area under a certain identical electrolyte condition. As suggested in a previous study,[S4] 0.035 mF/cm², was taken as the general specific capacitance in an acidic condition for a reasonable general value. The intrinsic catalytic activity was calculated by dividing the current by the specific surface area of the catalyst, which was estimated from the ECSA. Prior to the AST test, a stabilization protocol was applied at 1.1 V_{RHE} for 10 minutes. Subsequently, the OER stability was assessed by performing 3000 AST cycles

within a potential range of 1.23–1.63 V_{RHE} at a scan rate of 100 mV/sec. CA measurements were carried out at a constant potential of 1.58 V_{RHE} for 24 h. To evaluate catalytic activity, linear sweep voltammetry was conducted from 1.1–1.58 V_{RHE} right before CA tests at a scan rate of 10 mV/s.

The stability number (S-number) was obtained using the following equation.[S5,S6]

$$S\ \text{number} = \frac{n_{(O_2)}}{n_{(Ru)}}$$

where $n_{(O_2)}$ represents the number of moles of evolved O_2 during the OER, and $n_{(Ru)}$ is the moles of dissolved Ru in the electrolyte. To estimate the number of moles of evolved O_2, the current (i) during the test was integrated, as shown in the following equation:

$$n_{(O_2)} = \frac{1}{zF}\int i(t)\mathrm{d}t$$

where z is the number of electrons transferred during the OER ($z = 4$), F is the Faraday constant, and t is the duration time. To obtain $n_{(Ru)}$, the amounts of dissolved Ru (and foreign atoms) were quantified using inductively coupled plasma mass spectrometry (ICP-MS, PerkinElmer NexION1000 and Agilent 7700) after all AST and CA tests along with the following equation:

$$n_{(Ru)} = \frac{[Ru]\cdot V}{M_{Ru}}$$

where [Ru] is the concentration of Ru detected by ICP-MS, V is the volume of electrolyte, and M_{Ru} is the molar mass of Ru (101.07 g/mol).

Chronopotentiometry (CP) measurements were also performed at a current density of 10 mA/cm^2_{geo} using 0.5 mg/cm^2 of catalyst particles deposited on 3-mm glassy carbon rotating disk electrodes (GC-RDE, BAS Inc.) with acetylene black (Alfa Aesar). The catalyst-to-acetylene black mass ratio was adjusted to be 10:1. The electrode was rotated at 2400 rpm with an increase to 6000 rpm for 5 sec every 10 min to facilitate the removal of O_2 bubbles from the catalyst surface (RRDE-3A, ALS). For comparison of CP duration times among the synthesized catalyst oxides, RuO_2 (99.9%, anhydrous, Alfa Aesar) and RuO_2 (99.95%, anhydrous, Alfa Aesar) were used as reference catalysts. The average particle size of the former was approximately 37 nm, while that of the latter was 3 nm. The average particle size estimation was conducted using TEM.

Phase diagram reconstruction

The RuO_2–TiO_2 phase diagram presented in Figure 1a was adopted from Ref. 4 (*J. Phase Equilib. Diffus.* **29**, 136 (2008)) in the main text. In that study, Hardy's subregular solution model was employed to calculate the enthalpy of mixing, and the phase diagram was constructed by combining these calculations with available experimental measurements at specific temperatures. Based on both experimental and calculated data, the Gibbs energies for RuO_2 and TiO_2 were derived. These equations for the Gibbs energies were subsequently used to extend the phase diagram to lower temperatures. The binodal points at each temperature were estimated by applying a common tangent line, as exemplified in Supplementary Fig. S24.

DFT calculations

Ab initio DFT calculations were carried out to acquire the DOS and the isosurface of electron density difference of rutile-type oxides, utilizing the spin-polarized generalized-gradient approximation (GGA) along with the PBEsol functional optimized for exchange correlation of densely packed solids. The

ultrasoft pseudopotentials were utilized for ionic cores, as implemented in the CASTEP code (Biovia Inc.). Low-spin $(t_{2g}^4)(e_g^0)$ for the Ru^{4+} ($4d^4$) ions was assumed. The plane-wave basis set for the kinetic energy cutoff was set to 600 eV. Relaxation of the internal coordinates in the unit cell performed using the Broyden–Fletcher–Goldfarb–Shanno (BFGS) algorithm with convergence tolerances of 0.1 eV $Å^{-1}$ for the maximum ionic force, 5×10^{-5} eV/atom for the total energy, and 0.005 Å for the maximum ionic displacement.

Supplementary Tables and Figures

Table S1. Summary of dopants, electrochemical measurement conditions, and reported stability of RuO_2-based OER catalysts from previous literature

Catalyst	Dopant	Loading mass (mg/cm^2)	Electrolyte	Overpotential at 10 mA/cm^2 (mV)	Stability	Ref.
$Li_{0.52}RuO_2$	Li	0.637 mg_{Ru} cm^{-2}	0.5 M H_2SO_4	156	70 h @ 10 mA cm^{-2}	S7
B-RuO_2	B	-	0.5 M H_2SO_4	190	1000 h @ 10 mA cm^{-2} 200 h @ 4 A cm^{-2} (PEM)	S8
Ni,B-RuO_x	B, Ni	0.29	0.5 M H_2SO_4	206	700 h @ 10 mA cm^{-2} 200 h @ 0.5 A cm^{-2} (PEM)	S9
Ta/B-RuO_2	B, Ta	0.5	0.5 M H_2SO_4	170	80 h @ 10 mA cm^{-2} 120 h @ 0.2 A cm^{-2} (PEM)	S10
C-RuO_2-RuSe-5	C, Se	0.306 mg_{Ru} cm^{-2}	0.5 M H_2SO_4	221	30 h @ 10 mA cm^{-2}	S11
F–RuO_2/FC	F	0.075	0.5 M H_2SO_4	192	1440 h @ 1 A cm^{-2} (PEM)	S12
a/c-RuO_2	Na	0.404	0.1 M $HClO_4$	205	60 h @ 10 mA cm^{-2}	S13
Na–RuO_2	Na	2	0.1 M $HClO_4$	200	1800 h @ 10 mA cm^{-2} 225 h @ 0.5 A cm^{-2} (PEM)	S14
Mg–RuO_2 (350)	Mg	-	0.5 M H_2SO_4	228	30 h @ 10 mA cm^{-2}	S15
RuIrAl	Al, Ir	0.3	0.5 M H_2SO_4	178	300 h @ 0.1 A cm^{-2} 60 h @ 1 A cm^{-2} (PEM)	S16
Si-RuOx@C	Si	1.6	0.5 M H_2SO_4	220	100 h @ 10 mA cm^{-2}	S17
Si-RuO_2–0.1	Si	0.302	0.1 M $HClO_4$	226	800 h @ 10 mA cm^{-2}	S18
RuSiW	Si, W	0.65	0.5 M H_2SO_4	142	100 h @ 10 mA cm^{-2}	S19
$RuTiO_x$	Ti	-	0.5 M H_2SO_4	198	1400 h @ 50 mA cm^{-2} 100 h @ 0.5 A cm^{-2} (PEM)	S20
$Ru_{0.8}0Ti_{0.20}O_2$	Ti	0.025	0.1 M $HClO_4$	14 mA/mg_{cat} @ 1.51 V_{RHE}	-	S21
RuO_2/D-TiO_2	Ti	5	0.5 M H_2SO_4	180	100 h @ 0.2 A cm^{-2} (PEM)	S22
$Ru_{0.6}Cr_{0.2}Ti_{0.2}O_x$	Ti, Cr	0.5	0.5 M H_2SO_4	267 mV @ 0.1 A cm^{-2}	1100 h @ 10 mA cm^{-2} 210 h @ 0.1 A cm^{-2} (PEM)	S23
V_n–RuO_2	V	0.42	0.1 M $HClO_4$	270	1050 h @ 10 mA cm^{-2}	S24
GB-V-RuO_2	V	0.5	0.5 M H_2SO_4	159	760 h @ 10 mA cm^{-2} 500 h @ 0.2 A cm^{-2} (PEM)	S25
$Cr_{0.6}Ru_{0.4}O_2$	Cr	0.279	0.5 M H_2SO_4	178	10 h @ 10 mA cm^{-2}	S26
$Cr_{0.2}Ru_{0.8}O_{2-x}$	Cr	0.5	0.1 M $HClO_4$	170	2000 h @ 10 mA cm^{-2} 200 h @ 1 A cm^{-2} (PEM)	S27
ac-$Cr_{0.53}Ru_{0.47}O_{2-\delta}$	Cr	0.42	0.1 M $HClO_4$	239	40 h @ 10 mA cm^{-2}	S28
$Ru_{0.6}Cr_{0.4}O_2$	Cr	0.2	0.5 M H_2SO_4	195	20 h @ 10 mA cm^{-2} 12 h @ 0.1 A cm^{-2} (PEM)	S29
$Cr_{0.6}Ru_{0.4}O_2$	Cr	0.88	0.5 M H_2SO_4	220	500 h @ 50 mA cm^{-2} 350 h @ 0.3 A cm^{-2} (PEM)	S30
$Cr_{0.31}Ru_{0.69}O_2$	Cr	0.383	0.5 M H_2SO_4	176	1400 h @ 10 mA cm^{-2} 2300 h @ 0.3 A cm^{-2} (PEM)	S31
$Ru_3Cr_1Sr_{0.175}$	Cr, Sr	0.5	0.1 M $HClO_4$	214	300 h @ 10 mA cm^{-2}	S32
$RuIrFeCoCrO_2$	Cr, Fe, Co, Ir	0.2	0.5 M H_2SO_4	195	20 h @ 10 mA cm^{-2} 12 h @ 0.1 A cm^{-2} (PEM)	S33
Mn–RuO_2	Mn	0.275	0.5 M H_2SO_4	158	10 h @ 10 mA cm^{-2}	S34

$Mn_{0.73}Ru_{0.27}O_{2-\delta}$	Mn	0.28	0.5 M H_2SO_4	208	10 h @ 10 mA cm^{-2}	S35
$Mn_{0.2}RuO_2$	Mn	0.34	0.5 M H_2SO_4	188	180 h @ 0.2 A cm^{-2}	S36
$Mn_{0.4}Ru_{0.6}O_2$	Mn	1	1 M $HClO_4$	196	120 h @ 10 mA cm^{-2} 12 h @ 1 A cm^{-2} (PEM)	S37
Mn–RuO_2 NFs/M	Mn	0.252	0.5 M H_2SO_4	143	480 h @ 10 mA cm^{-2}	S38
Post-0.8 V $RuMnO_x$	Mn	-	0.5 M H_2SO_4	247	2600 h @ 10 mA cm^{-2}	S39
Mn_xRu_{1-x}/MnO_2/CFs	Mn	0.89	0.1 M $HClO_4$	161	600 h @ 10 mA cm^{-2} 24 h @ 0.5 A cm^{-2} (PEM)	S40
$Mn_{0.2}Ru_{0.8}O_2$	Mn	-	0.5 M H_2SO_4	214	50 h @ 10 mA cm^{-2} 100 h @ 0.2 A cm^{-2} (PEM)	S41
$MnRuO_x$-300	Mn	0.2	0.5 M H_2SO_4	307	780 h @ 0.1 A cm^{-2} 80 h @ 0.1 A cm^{-2} (PEM)	S42
$Mn_{(SA)}/RuO_2$	Mn	0.51	0.5 M H_2SO_4	284	1000 h @ 10 mA cm^{-2} 180 h @ 1 A cm^{-2} (PEM)	S43
$Ru_{0.5}Mn_{0.5}O_2$	Mn	0.35	0.5 M H_2SO_4	166	2500 h @ 10 mA cm^{-2} 600 h @ 0.2 A cm^{-2} (PEM)	S44
$Nb_{0.1}Mn_{0.1}Ru_{0.8}O_2$	Mn, Nb	0.4	0.5 M H_2SO_4	209	200 h @ 10 mA cm^{-2} 1000 h @ 0.5 A cm^{-2} (PEM)	S45
S-$RuFeO_x$	Fe	10 ug_{Ru} cm^{-2}	0.1 M $HClO_4$	187	50 h at 1 mA cm^{-2}	S46
$Co_{0.11}Ru_{0.89}O_{2-\delta}$	Co	0.283	0.5 M H_2SO_4	169	50 h @ 10 mA cm^{-2}	S47
$RuCoO_x$	Co	0.0428 mg_{Ru} cm^{-2}	1 M $HClO_4$	200	100 h @ 10 mA cm^{-2} 10 h @ 0.1 A cm^{-2} (PEM)	S48
$RuCo/RuCoO_x$	Co	0.35	0.5 M H_2SO_4	170	2500 h @ 10 mA cm^{-2} 200 h @ 0.2 A cm^{-2} (PEM)	S49
$Co_{0.3}Ru_{0.7}O_2$–TiO_2	Co	1	0.5 M H_2SO_4	153	410 h @ 0.1 A cm^{-2} 1060 h @ 0.5 A cm^{-2} (PEM)	S50
Co–RuO_2	Co	0.2	0.5 M H_2SO_4	~300	1000 h @ 10 mA cm^{-2} 2000 h @ 1 A cm^{-2} (PEM)	S51
PtCo-RuO_2/C	Co, Pt	20 ug_{Ru+Pt} cm^{-2}	0.1 M $HClO_4$	213	20 h @ 10 mA cm^{-2} 24 h @ 1 A cm^{-2} (PEM)	S52
RuO_2-HEAE	Co, Ni, Cu, Mn, Sm	0.5	0.1 M $HClO_4$	201	1500 h @ 0.1 A cm^{-2} 1500 h @ 1 A cm^{-2} (PEM)	S53
Ni-RuO_2	Ni	0.4	0.1 M $HClO_4$	214	200 h @ 10 mA cm^{-2} 1000 h @ 0.2 A cm^{-2} (PEM)	S54
$Ru_{(SA)}$-NiOMS	Ni, Mn	0.1	0.5 M H_2SO_4	160	300 h @ 10 mA cm^{-2} 100 h @ 0.1 A cm^{-2} (PEM)	S55
Cu-doped RuO_2	Cu	0.275	0.5 M H_2SO_4	188	8 h @ 10 mA cm^{-2}	S56
$Ru_{0.85}Zn_{0.15}O_{2-\delta}$	Zn	0.416	0.5 M H_2SO_4	190	50 h @ 10 mA cm^{-2}	S57
py-RuO_2:Zn	Zn	6.0 μmol cm^{-2}	0.5 M H_2SO_4	173	1000 h @ 10 mA cm^{-2}	S58
SA Zn–RuO_2	Zn	0.47	0.1 M $HClO_4$	210	43 h @ 10 mA cm^{-2}	S59
$ZnRuO_x$	Zn	0.255	0.5 M H_2SO_4	255	320 h @ 10 mA cm^{-2} 120 h @ 0.2 A cm^{-2} (PEM)	S60
E–Zn–RuO_2	Zn	0.354	0.5 M H_2SO_4	190	60 h @ 10 mA cm^{-2}	S61
Zn-RuO_2@ZnO	Zn	4	0.5 M H_2SO_4	170	600 h @ 10 mA cm^{-2} 100 h @ 1 A cm^{-2} (PEM)	S62
Ga–RuO_2	Ga	0.09	0.5 M H_2SO_4	217.5	150 h @ 10 mA cm^{-2}	S63

$Sr_{0.1}RuO_x$	Sr	-	0.5 M H_2SO_4	201	100 h @ 10 mA cm^{-2} 240 h @ 10 mA cm^{-2} (PEM)	S64
TS-$Sr_{0.1}Ta_{0.1}Ru_{0.8}O_{2-x}$	Sr, Ta	1	0.5 M H_2SO_4	166	1000 h @ 10 mA cm^{-2} 400 h @ 0.5 A cm^{-2}	S65
ZrO_2–RuO_2	Zr	-	0.5 M H_2SO_4	170	1800 h @ 10 mA cm^{-2} 100 h @ 2 A cm^{-2} (PEM)	S66
$Ru_{0.87}Zr_{0.13}O_2$	Zr	0.0255	0.1 M $HClO_4$	19 mA/mg_{cat} @ 1.51 V_{RHE}	-	S67
$Nb_{0.1}Ru_{0.9}O_2$	Nb	0.51	0.5 M H_2SO_4	204	360 h @ 0.2 A cm^{-2} 100 h @ 0.3 A cm^{-2} (PEM)	S68
Ru_3MoCeO_x	Mo, Ce	0.3	0.5 M H_2SO_4	164	100 h @ 0.1 A cm^{-2}	S69
$Mo_{0.15}$-RuO_2	Mo	0.23	0.5 M H_2SO_4	147	20 h @ 10 mA cm^{-2}	S70
RuO_2/MoO_3	Mo	0.563	0.5 M H_2SO_4	167	300 h @ 10 mA cm^{-2}	S71
Rh-RuO_2	Rh	0.45	0.5 M H_2SO_4	161	700 h @ 50 mA cm^{-2}	S72
$In_{0.17}Ru_{0.83}O_2$-350	In	0.275	0.5 M H_2SO_4	177	20 h @ 10 mA cm^{-2}	S73
In-RuO_2/G	In	0.28	0.5 M H_2SO_4	187	350 h @ 0.1 A cm^{-2} (PEM)	S74
$SnRuO_x$	Sn	0.4165	0.5 M H_2SO_4	194	250 h @ 0.1 mA cm^{-2} 1300 h @ 1 A cm^{-2} (PEM)	S75
$RuSnO_x$	Sn	0.2	0.1 M $HClO_4$	184	150 h @ 10 mA cm^{-2}	S76
$Ru_{0.8}Sb_{0.2}O_2$	Sb	-	0.5 M H_2SO_4	160	1100 h @ 10 mA cm^{-2} 500 h @ 1 A cm^{-2} (PEM)	S77
Sb-RuO_2	Sb	2	0.5 M H_2SO_4	220	1200 h @ 10 mA cm^{-2} 100 h @ 1 A cm^{-2} (PEM)	S78
$Ba_{0.3}(SO_4)_\delta W_{0.2}Ru_{0.5}O_{2-\delta}$	Ba, W	0.125	0.5 M H_2SO_4	206	1000 h @ 10 mA cm^{-2} 300 h @ 0.5 A cm^{-2} (PEM)	S79
Ce@RuO_2/CoNC	Ce	0.32	0.5 M H_2SO_4	190	1000 h @ 10 mA cm^{-2}	S80
RuO_2–CeO_2–CC	Ce	-	0.5 M H_2SO_4	180	1000 h @ 10 mA cm^{-2}	S81
$Nd_{0.1}RuO_x$/CC	Nd	-	0.5 M H_2SO_4	211	50 h @ 10 mA cm^{-2}	S82
Nd-RuO_2	Nd	-	0.5 M H_2SO_4	200	70 h @ 10 mA cm^{-2}	S83
Sm–RuO_{2-x}–O_v	Sm	0.707	0.5 M H_2SO_4	217	320 h @ 10 mA cm^{-2}	S84
Er-RuO_x	Er	0.5	0.5 M H_2SO_4	200	200 h @ 10 mA cm^{-2} 100 h @ 1 A cm^{-2}	S85
Ta-RuO_2	Ta	0.416	0.1 M $HClO_4$	201	280 h @ 10 mA cm^{-2}	S86
$Ta_{0.1}Ru_{0.9}O_{2-x}$	Ta	0.25	0.5 M H_2SO_4	226	2800 h @ 1 A cm^{-2} (PEM)	S87
Ta_1/RuO_2	Ta	0.35	0.5 M H_2SO_4	164	1000 h @ 0.1 A cm^{-2} 650 h @ 0.5 A cm^{-2} (PEM)	S88
90%RuO_2–10%Ta_2O_5	Ta	1.5	1.0 H_3PO_4	9.13 mA cm^{-2} @ 1.2 $V_{Ag/AgCl}$	5 h @ 1.1 A cm^{-2} (PEM)	S89
Ta-RuO_2	Ta	1.1	0.5 M H_2SO_4	202	50 h @ 10 mA cm^{-2}	S90
$W_{0.2}Er_{0.1}Ru_{0.7}O_{2-\delta}$	W, Er	0.33	0.5 M H_2SO_4	168	500 h @ 10 mA cm^{-2} 120 h @ 0.1 A cm^{-2} (PEM)	S91
$Ru_5W_1O_x$	W	0.0225	0.5 M H_2SO_4	227	550 h @ 10 mA cm^{-2}	S92

$(Ru–W)O_x$	W	-	0.5 M H_2SO_4	170	300 h @ 10 mA cm^{-2} 50 h @ 1 A cm-2 (PEM)	S93
$W\text{-}IrRu_3O_x$	W, Ir	0.32	0.5 M H_2SO_4	249	500 h @ 10 mA cm^{-2} 24 h @ 1.5 A cm^{-2} (PEM)	S94
$Re_{0.06}Ru_{0.94}O_2$	Re	0.1	0.1 M $HClO_4$	190	200 h @ 10 mA cm^{-2}	S95
$Ir_{0.6}Ru_{0.4}O_2$	Ir	2	-	1 A cm^{-2} @ 1.567 V (PEM)	-	S96
$Ru_{0.5}Ir_{0.5}O_2$	Ir	0.283	0.5 M H_2SO_4	151	618.3 h @ 10 mA cm^{-2} 255 h @ 0.2 A cm^{-2} (PEM)	S97
$Ir_{0.4}Ru_{0.6}O_2$	Ir	0.075	0.5 M H_2SO_4	~300	5 h @ 10 mA cm^{-2}	S98
Ir-RuO_2	Ir	1	0.5 M H_2SO_4	167	1023 h @ 10 mA cm^{-2} 300 h @ 1 A cm^{-2} (PEM)	S99
Ru_6IrO_x	Ir	0.4	0.1 M $HClO_4$	240	1500 h @ 2 A cm^{-2} (PEM)	S100
SS Pt-RuO_2 HNSs	Pt	0.306	0.5 M H_2SO_4	228	100 h @ 10 mA cm^{-2} 100 h @ 0.1 A cm^{-2} (PEM)	S101
Pt-RuO_2	Pt	2.5	0.5 M H_2SO_4	215	1500 h @ 10 mA cm^{-2} 500 h @ 0.5 A cm^{-2} (PEM)	S102
Pb-RuO_2	Pb	0.5	0.5 M H_2SO_4	188	1100 h @ 10 mA cm^{-2} 250 h @ 0.5 A cm^{-2} (PEM)	S103
Bi-RuO_2 SAAO	Bi	1	0.5 M H_2SO_4	192	650 h @ 10 mA^{-2} 24 h @ 0.2 A cm^{-2} (PEM)	S104

Table S2. EXAFS fitting parameters at the Ru *K*-edge for samples containing Fe, Co, Ni, and Cu

Nanocrystals	Shell	CN	R (Å)	σ^2 (Å^2)	ΔE_0 (eV)	R factor
$(Ru_{0.8}Fe_{0.2})O_2$	Ru–O (1)	2.0	2.07	0.0003	-0.4	0.028
	Ru–O (2)	4.0	1.95			
$(Ru_{0.8}Co_{0.2})O_2$	Ru–O (1)	2.1	2.05	0.0002	1.5	0.030
	Ru–O (2)	4.1	1.93			
$(Ru_{0.8}Ni_{0.2})O_2$	Ru–O (1)	2.1	2.06	0.0001	3.3	0.017
	Ru–O (2)	4.1	1.94			
$(Ru_{0.8}Cu_{0.2})O_2$	Ru–O (1)	2.0	1.92	0.0005	3.5	0.019
	Ru–O (2)	4.1	2.03			

CN, coordination number; R, the distance between absorber and backscatter atoms; σ^2, Debye-Waller factor to account for both thermal and structural disorders; $\Delta E_{0,}$ inner potential correction; R-factor indicates the goodness of the fit. S_0^2 was fixed as 0.837 according to the experimental EXAFS fit of commercial RuO_2

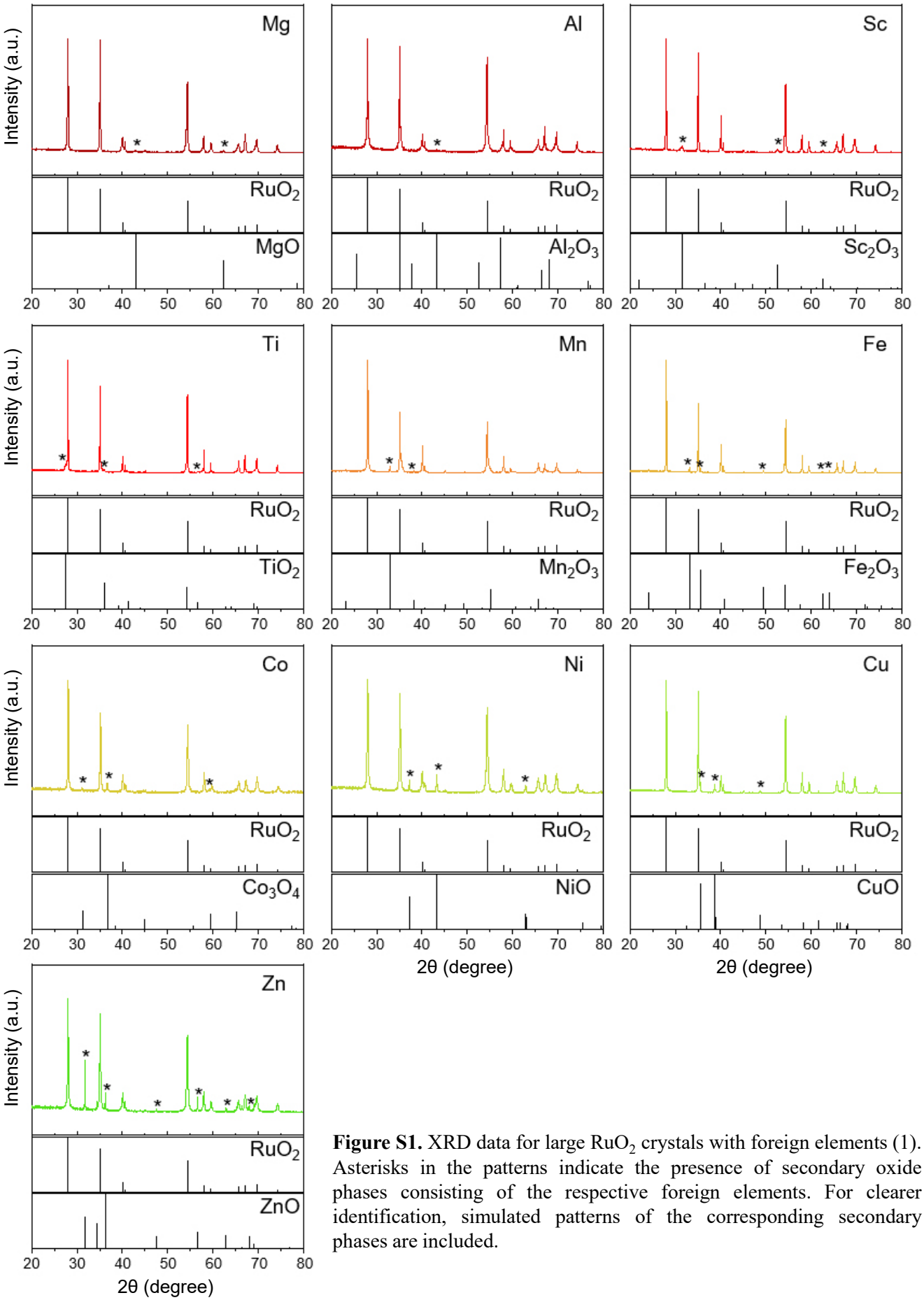

Figure S1. XRD data for large RuO_2 crystals with foreign elements (1). Asterisks in the patterns indicate the presence of secondary oxide phases consisting of the respective foreign elements. For clearer identification, simulated patterns of the corresponding secondary phases are included.

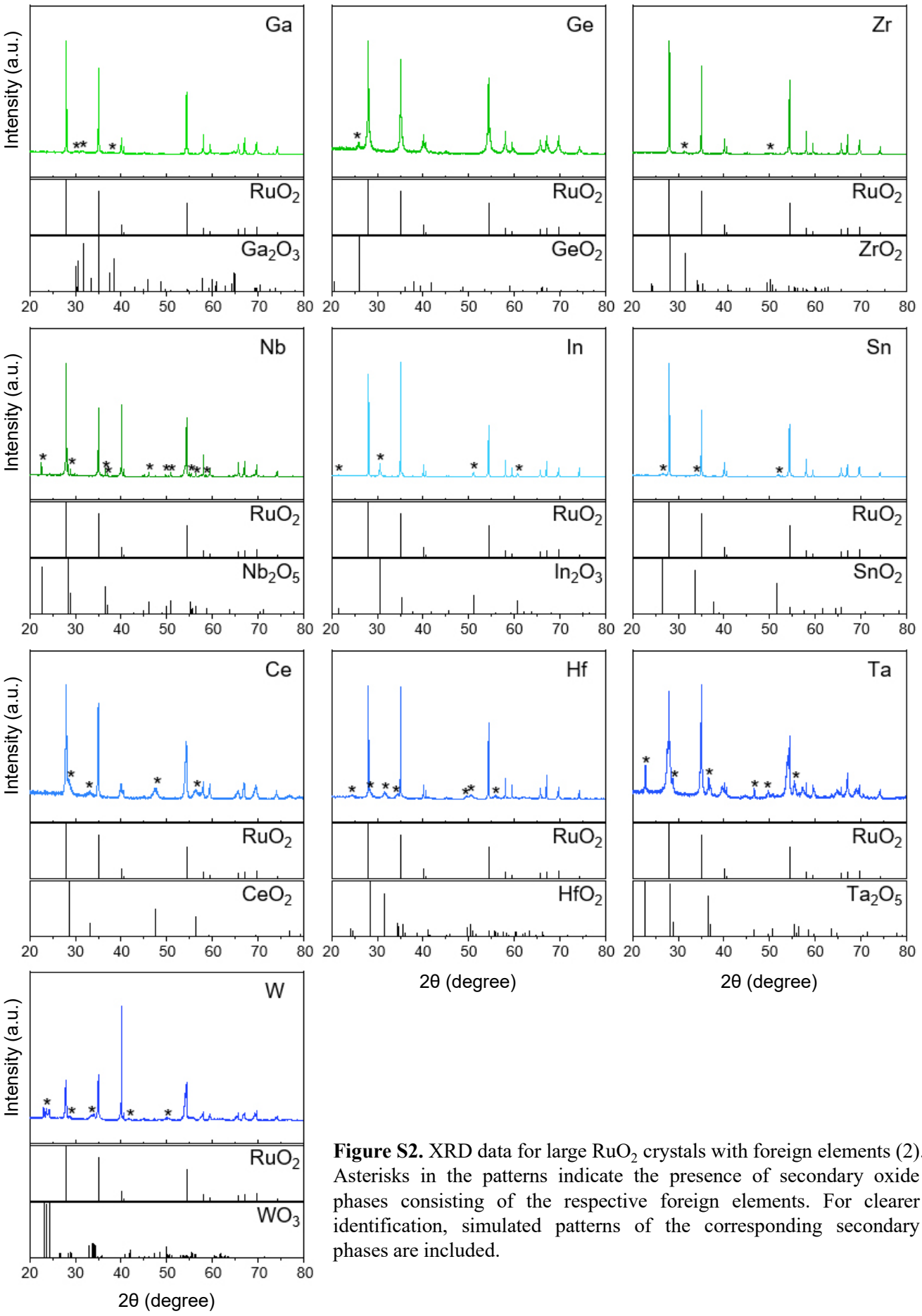

Figure S2. XRD data for large RuO_2 crystals with foreign elements (2). Asterisks in the patterns indicate the presence of secondary oxide phases consisting of the respective foreign elements. For clearer identification, simulated patterns of the corresponding secondary phases are included.

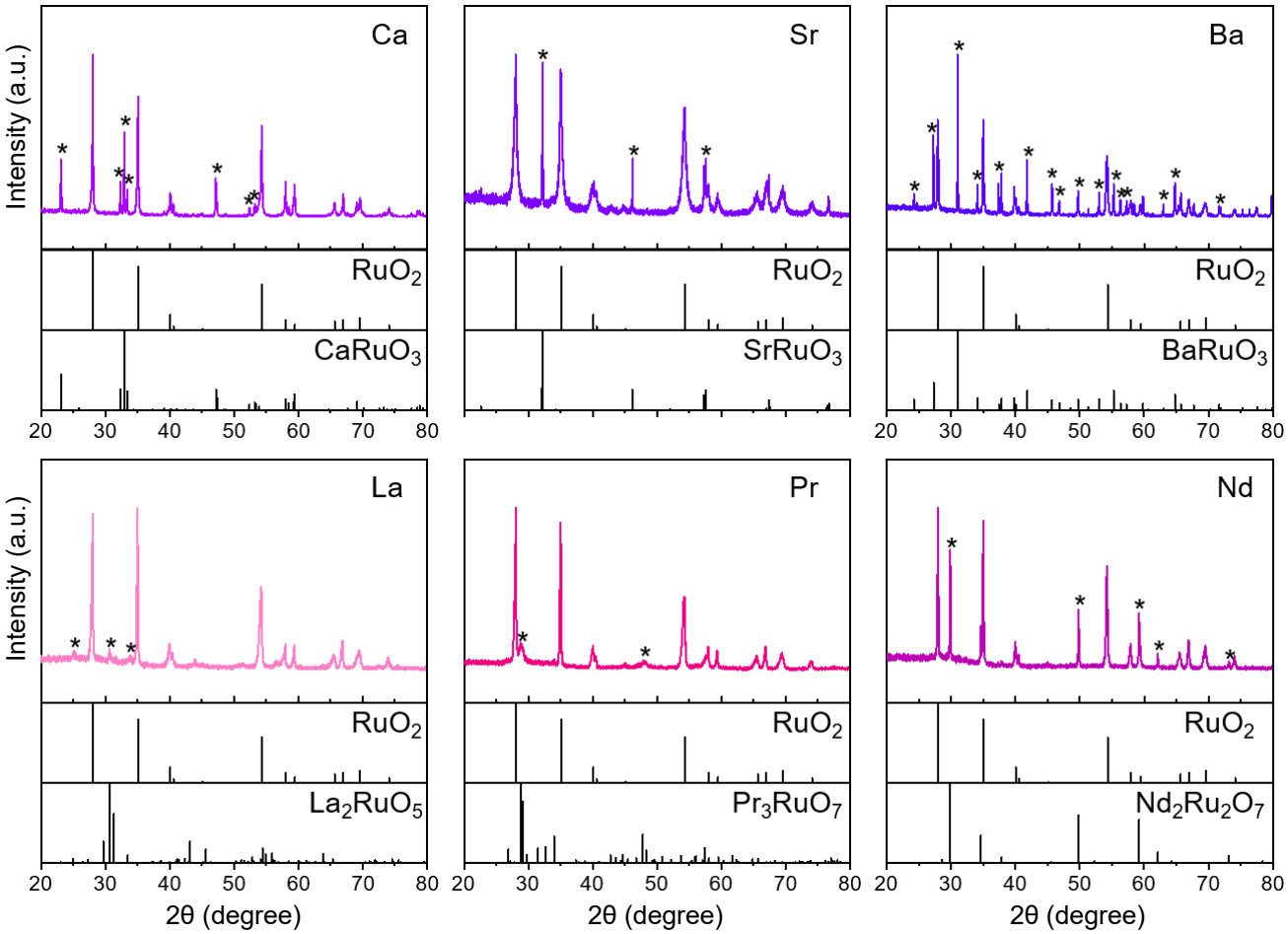

Figure S3. XRD data for large RuO_2 crystals with foreign elements (3). Asterisks in the patterns indicate the presence of secondary intermediate phases based on ruthenates. For clearer identification, simulated patterns of the corresponding secondary ruthenate phases are included.

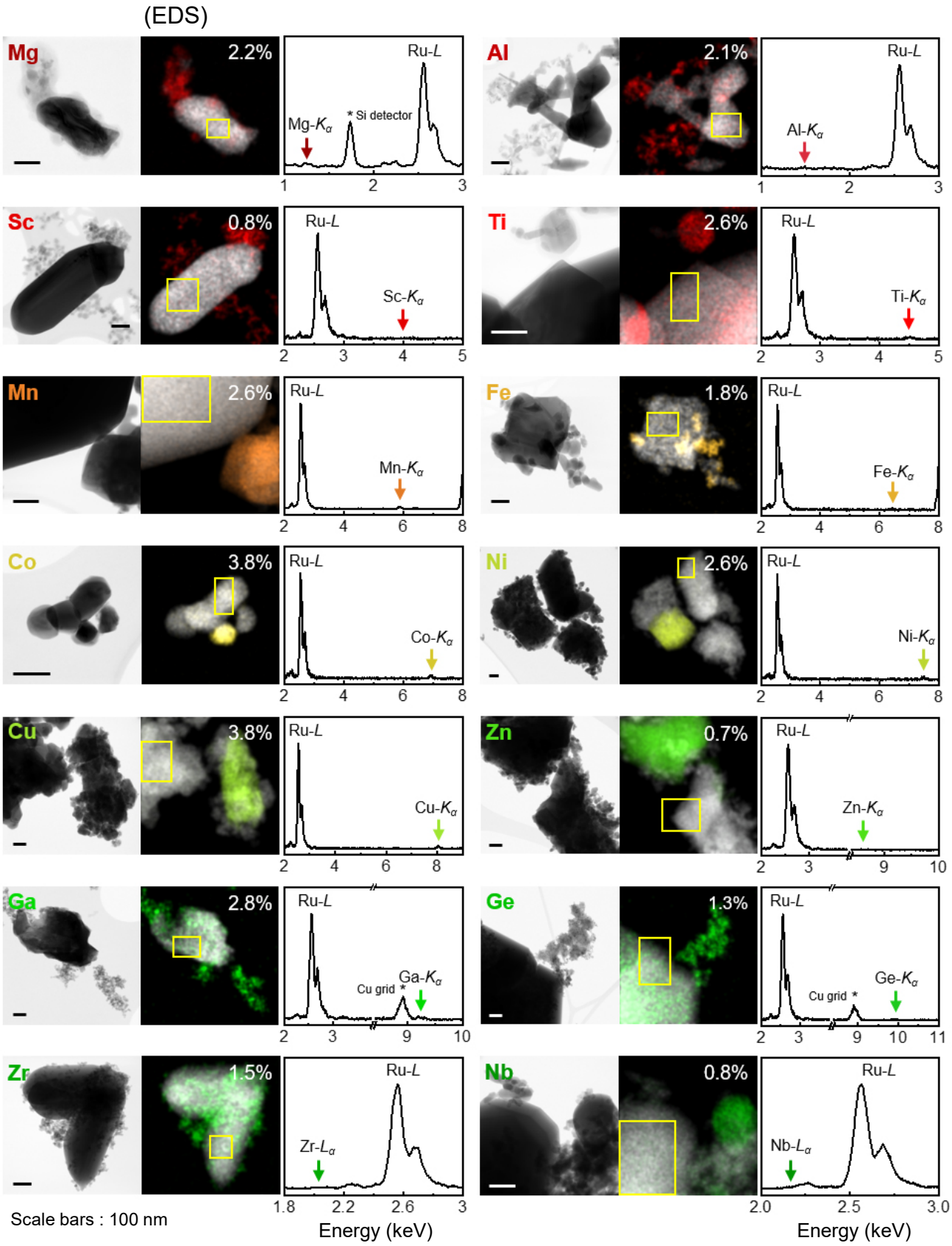

Figure S4. EDS maps and spectra for large RuO_2 crystals with foreign elements (1). In addition to visualizing the presence of second-phase particles in the EDS maps, the concentration of foreign elements in RuO_2 crystals was quantified using the EDS spectra. The spectra were obtained from the regions indicated by yellow rectangles in the maps. The numerical data on the maps represent the concentrations of the foreign elements estimated from the spectra.

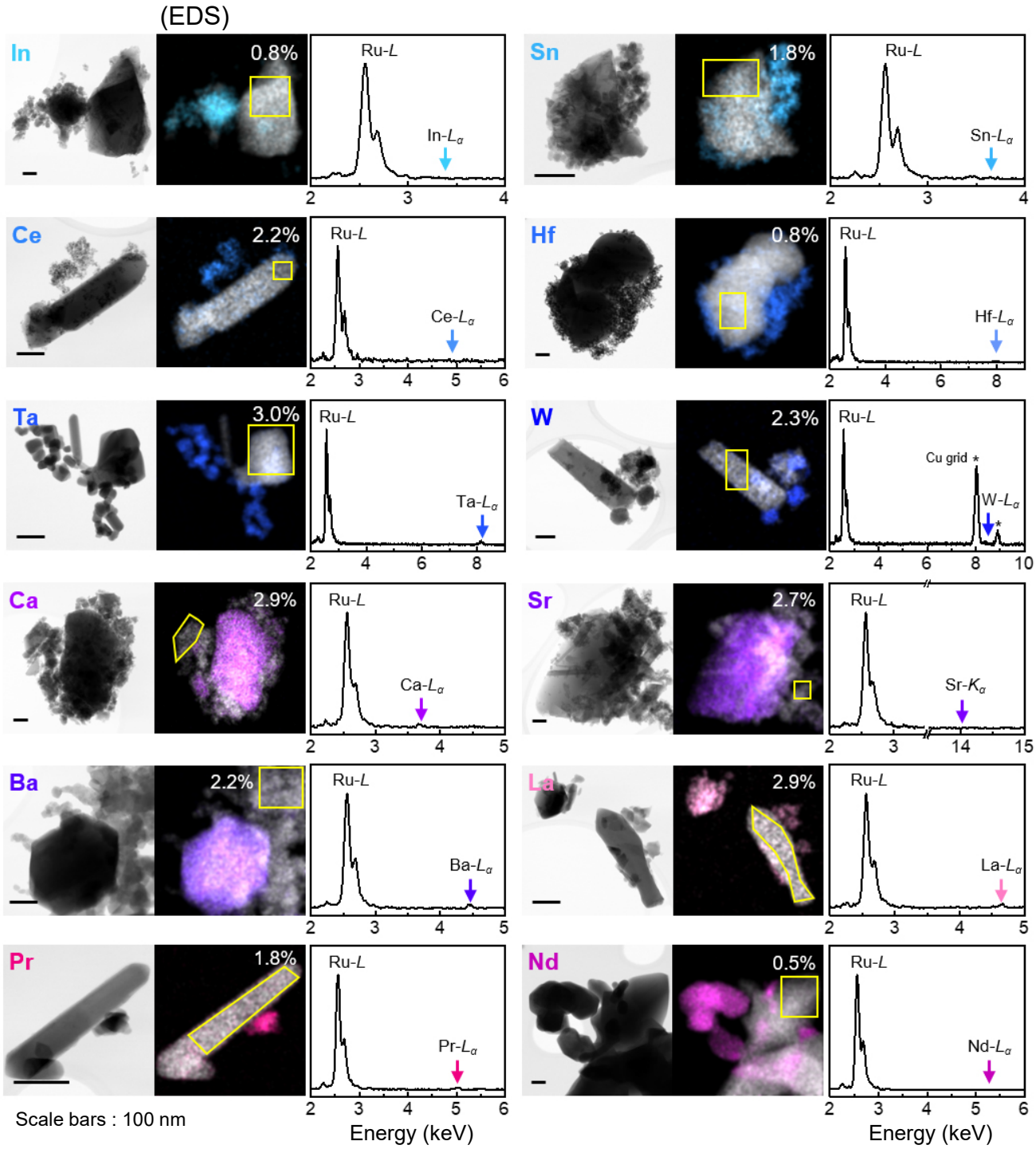

Figure S5. EDS maps and spectra for large RuO_2 crystals with foreign elements (2). In addition to visualizing the presence of second-phase particles in the EDS maps, the concentration of foreign elements in RuO_2 crystals was quantified using the EDS spectra. The spectra were obtained from the regions indicated by yellow rectangles in the maps. The numerical data on the maps represent the concentrations of the foreign elements estimated from the spectra.

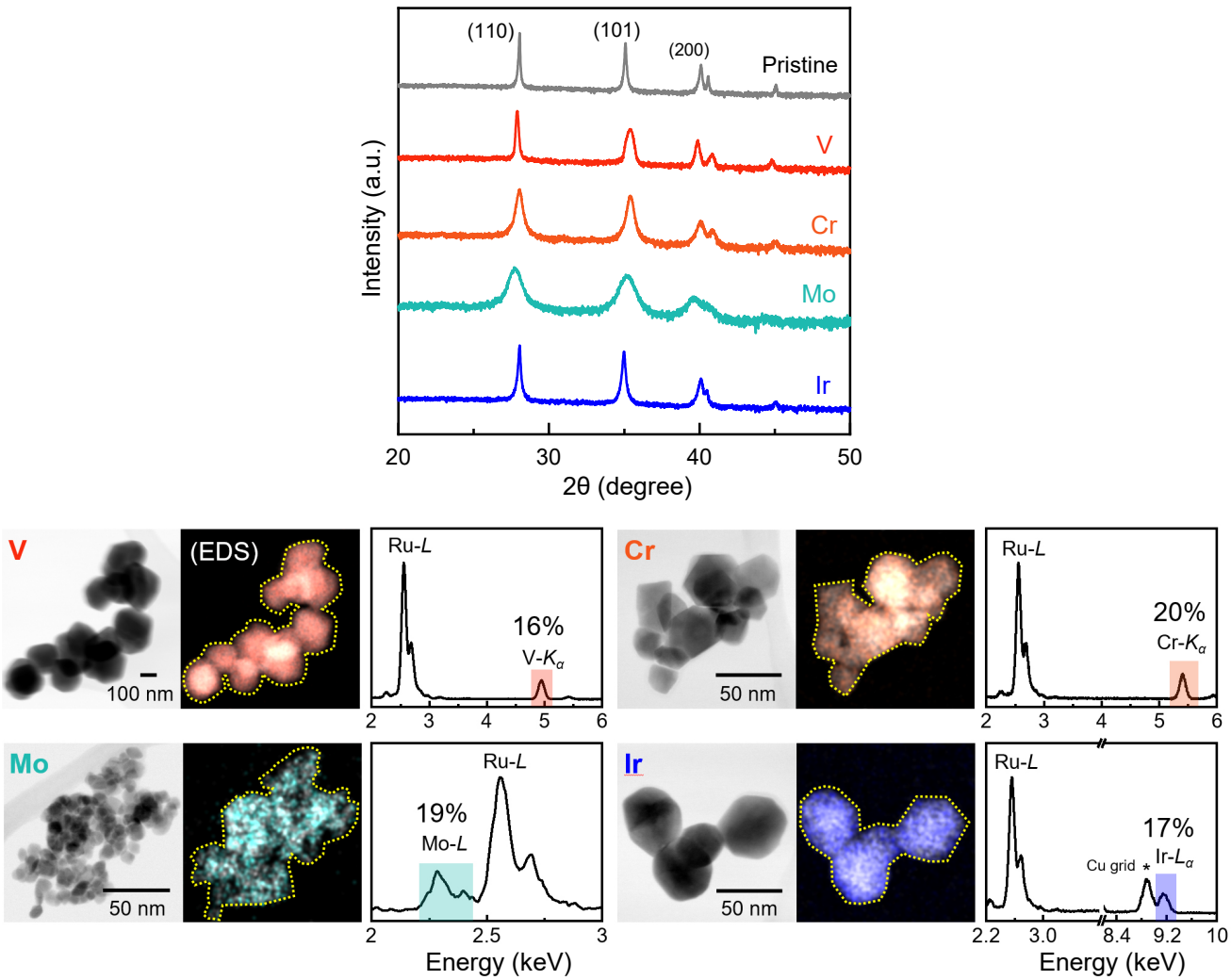

Figure S6. XRD patterns, compositional maps, and EDS spectra for RuO_2 crystals containing V, Cr, Mo, and Ir. Among 30 elements, these four, each at 20 at%, are identified as being soluble in RuO_2, regardless of crystal size. IrO_2 is already known to from a solid solution with RuO_2 across a full composition range. The absence of additional Bragg reflections in the XRD patterns, along with the EDS maps and spectra, directly verifies the formation of solid solutions incorporating these four elements.

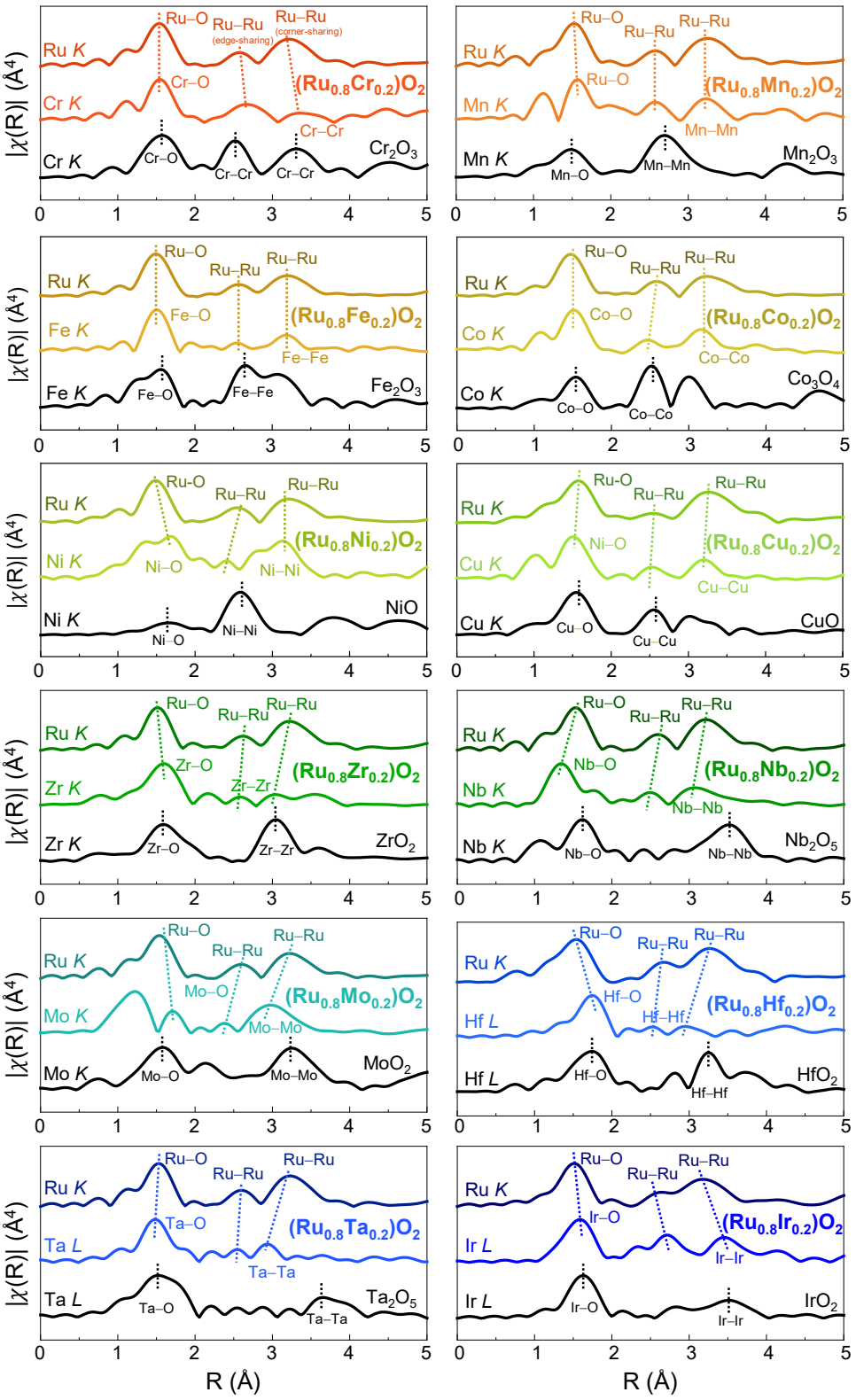

Figure S7. EXAFS analysis data (1). The analysis demonstrates that the M–O and M–M radial distances in the samples containing M (Cr, Mn, Fe, Co, Ni, Cu, Zr, Nb, Mo, Hf, Ta, and Ir) align with the Ru–O and Ru–Ru distances in RuO_2. These EXAFS results thus consistently support the formation of solid solutions.

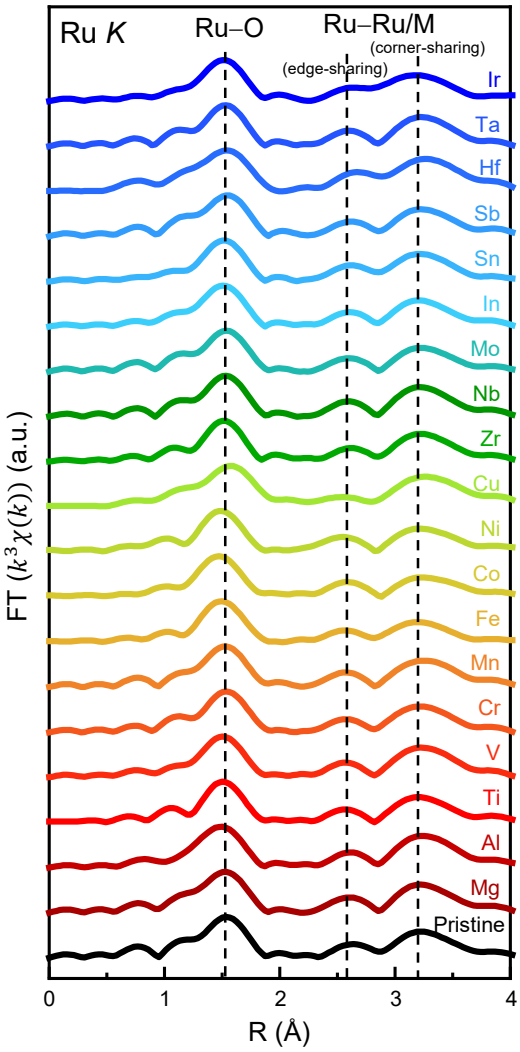

Figure S8. EXAFS analysis data (2). The analysis demonstrates that the Ru–O and Ru–Ru/M radial distances in the solid-solution samples containing M align with the Ru–O and Ru–Ru distances in RuO_2. These EXAFS results thus consistently support the formation of solid solutions.

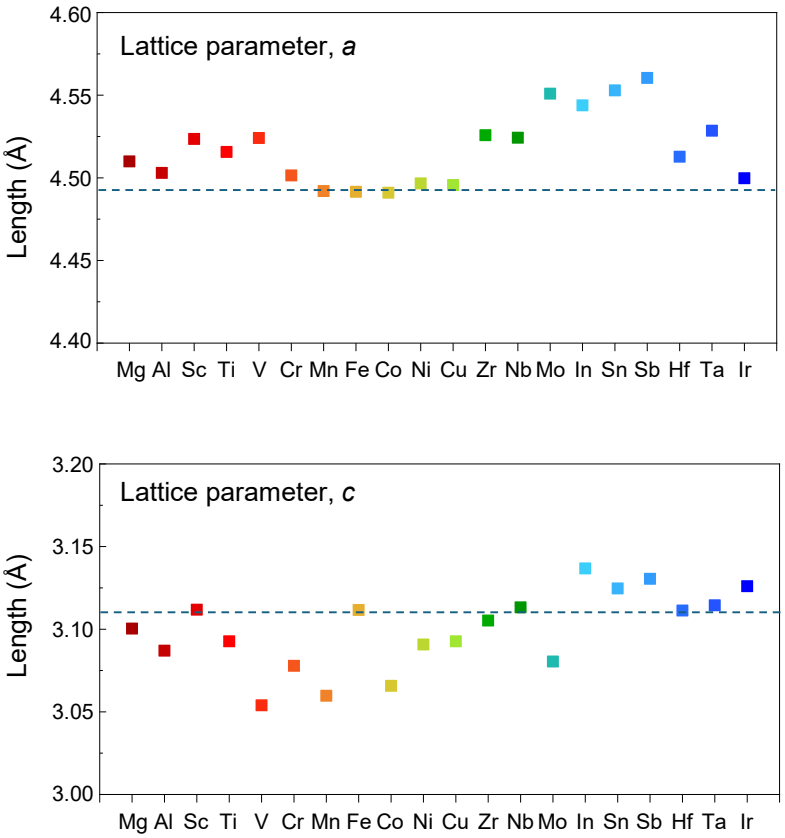

Figure S9. Lattice parameters of solid solutions. The lattice parameters, *a* and *c*, of the rutile-type solid solutions were obtained from the XRD data shown in Figure 2 in the main text. Anisotropic expansion and contractions of *a* and *c* appear to be a common feature of the solid solutions. The horizontal dashed lines in the plots indicate the lattice parameters of pristine RuO_2, as reported from the powder diffraction file (PDF) data-base (PDF card no. 01-088-0322).

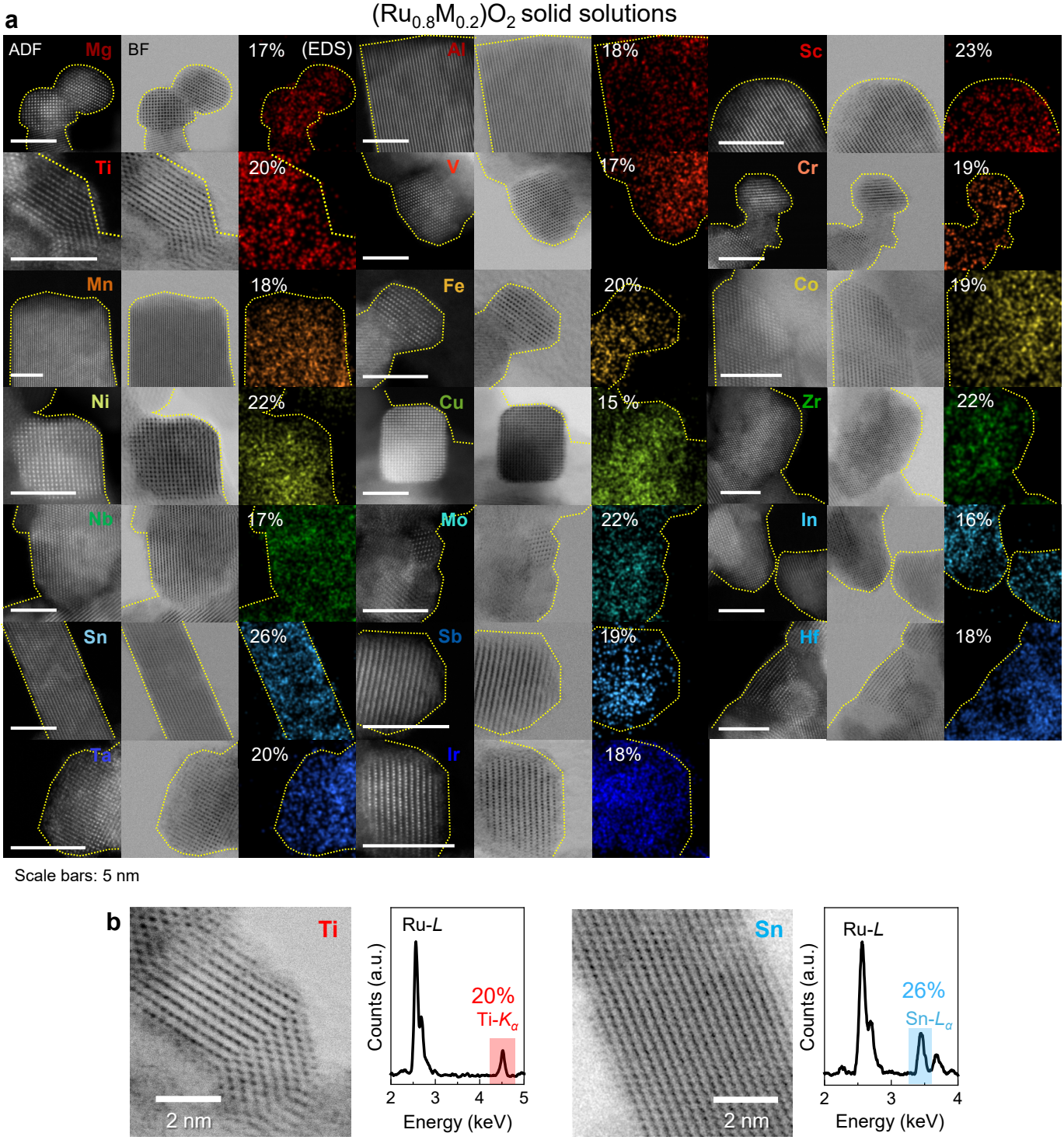

Figure S10. Additional EDS composition maps visualizing the solid solutions of $Ru_{0.8}M_{0.2}O_2$. (**a**) The EDS maps directly confirm the incorporation of foreign elements into the nanocrystals. The numerical data on the maps indicate the substitution concentration of each foreign element at the Ru sites. (**b**) All the substitution concentrations are obtained from the corresponding EDS spectra. Two representative cases (Ti and Sn) consistently show substantial signal intensity, verifying their presence in the solid solution.

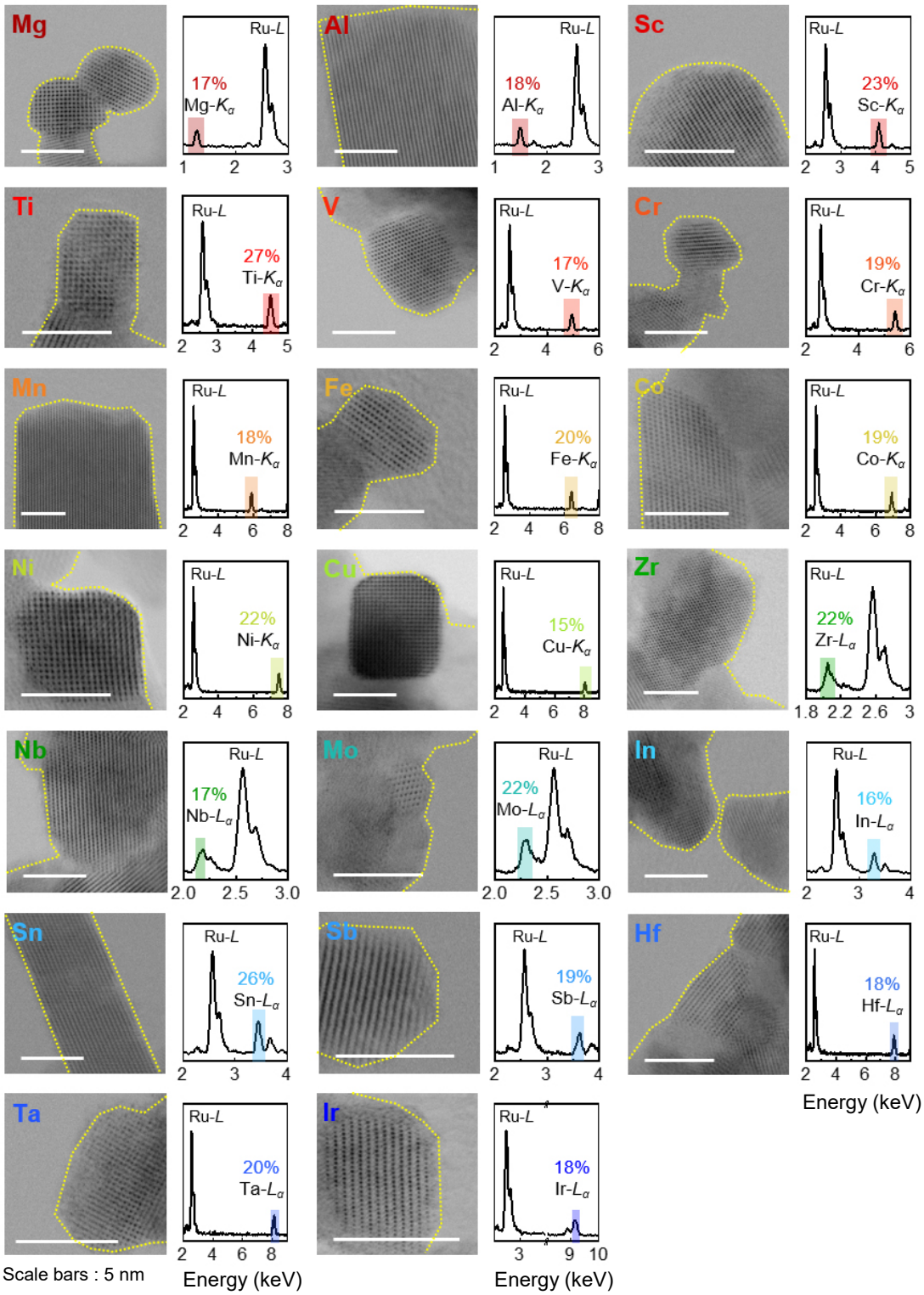

Figure S11. BF images and EDS spectra of solid-solution nanocrystals. The numeric values in the EDS spectra indicate the amounts of foreign elements detected within nanocrystals by EDS, confirming their presence as substituted elements in the solid solutions.

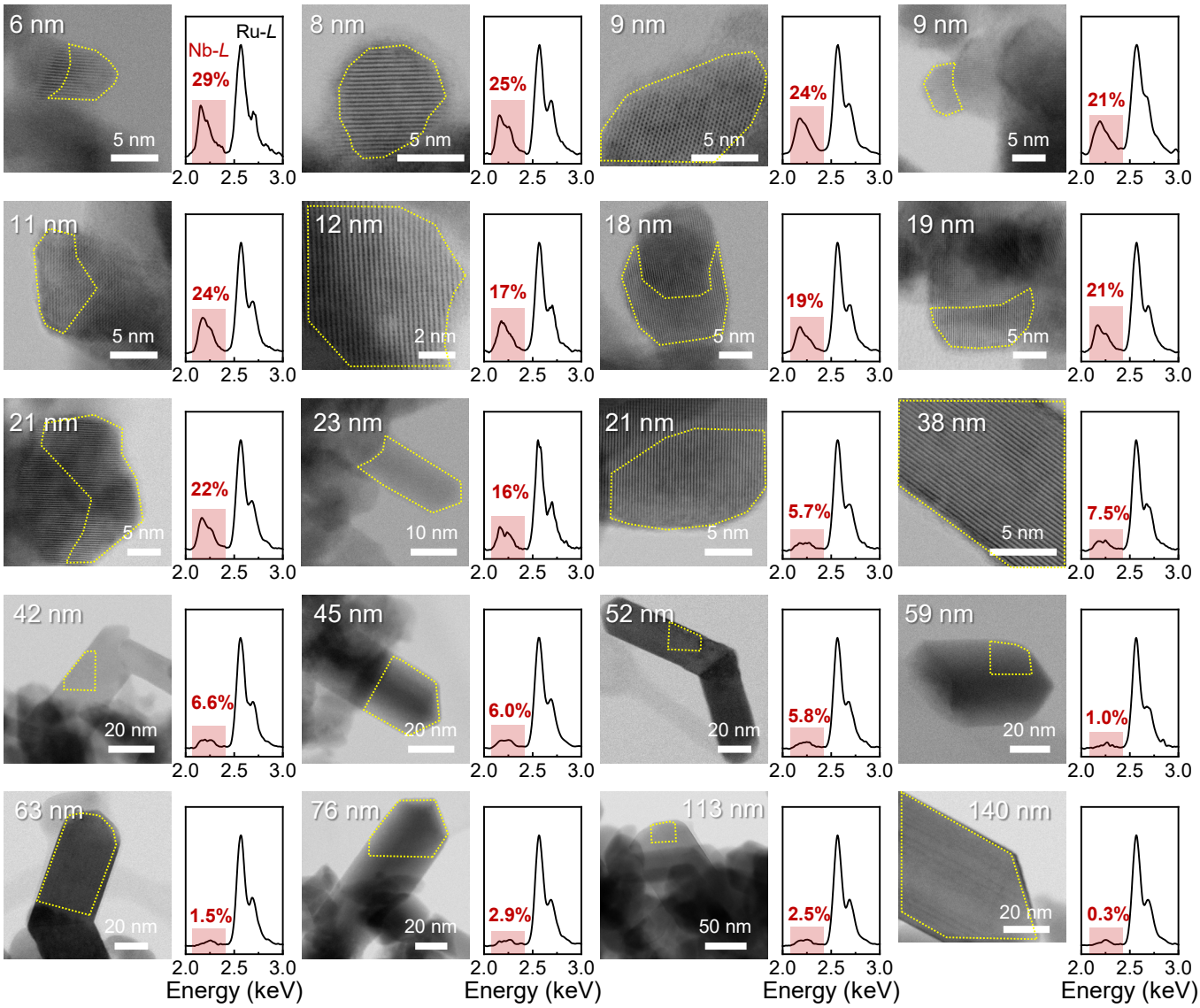

Figure S12. BF images of crystals and their EDS spectra in the sample with Nb added. The images are arranged in order of increasing crystal size, as indicated in each image. Each spectrum was acquired from a single crystalline region outlined by a yellow curve. As the crystal size exceeds 20 nm, the Nb concentration detected by EDS significantly decreases to less than 10 at%. The Nb-*L* line in the spectra is highlighted with light red shading.

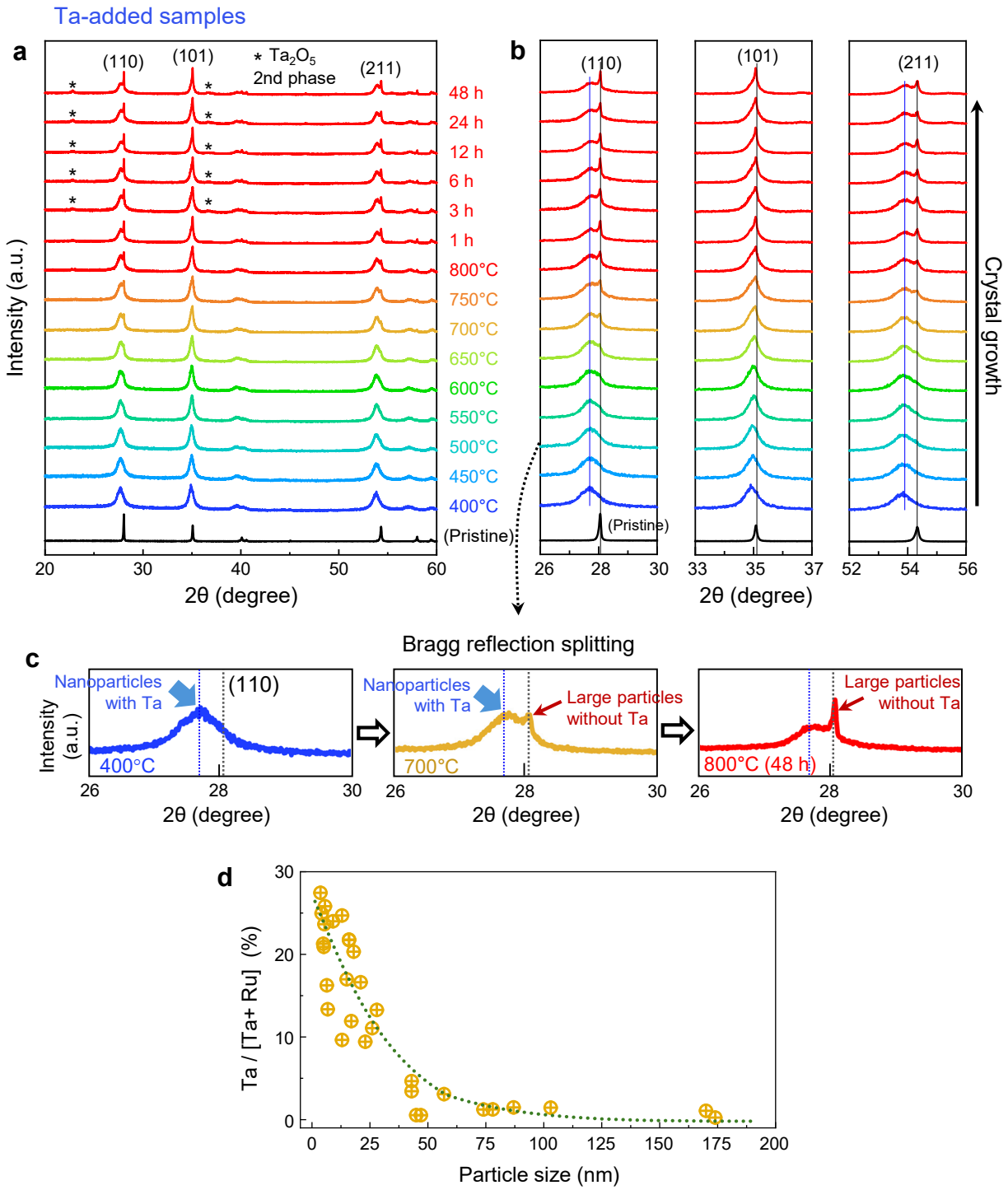

Figure S13. Crystal-size-dependent XRD patterns and composition variation in samples with Ta. (**a**) A series of XRD patterns was collected for samples annealed between 400 and 800°C. The secondary Ta_2O_5 phase appears at 800°C. (**b**) Three major Bragg reflections are magnified to clarify the peak variations. Consistent with the case of Nb samples, peak splitting is observed for the (110) and (211) reflections at 700°C and above. (**c**) Magnified views of the (110) reflection at three temperatures demonstrate similar phase evolution to that of the Nb samples: nanoscale solid-solution $Ru_{0.8}Ta_{0.2}O_2$ crystals at 400°C; a mixture of solid-solution $Ru_{0.8}Ta_{0.2}O_2$ nanocrystals and larger RuO_2 crystals with negligible Nb content at 700°C; and large RuO_2 crystals alongside a Ta_2O_5 secondary phase after 48 h at 800°C. (**d**) This plot shows Ta concentrations derived from the EDS spectra of individual crystals in the sample annealed at 700°C.

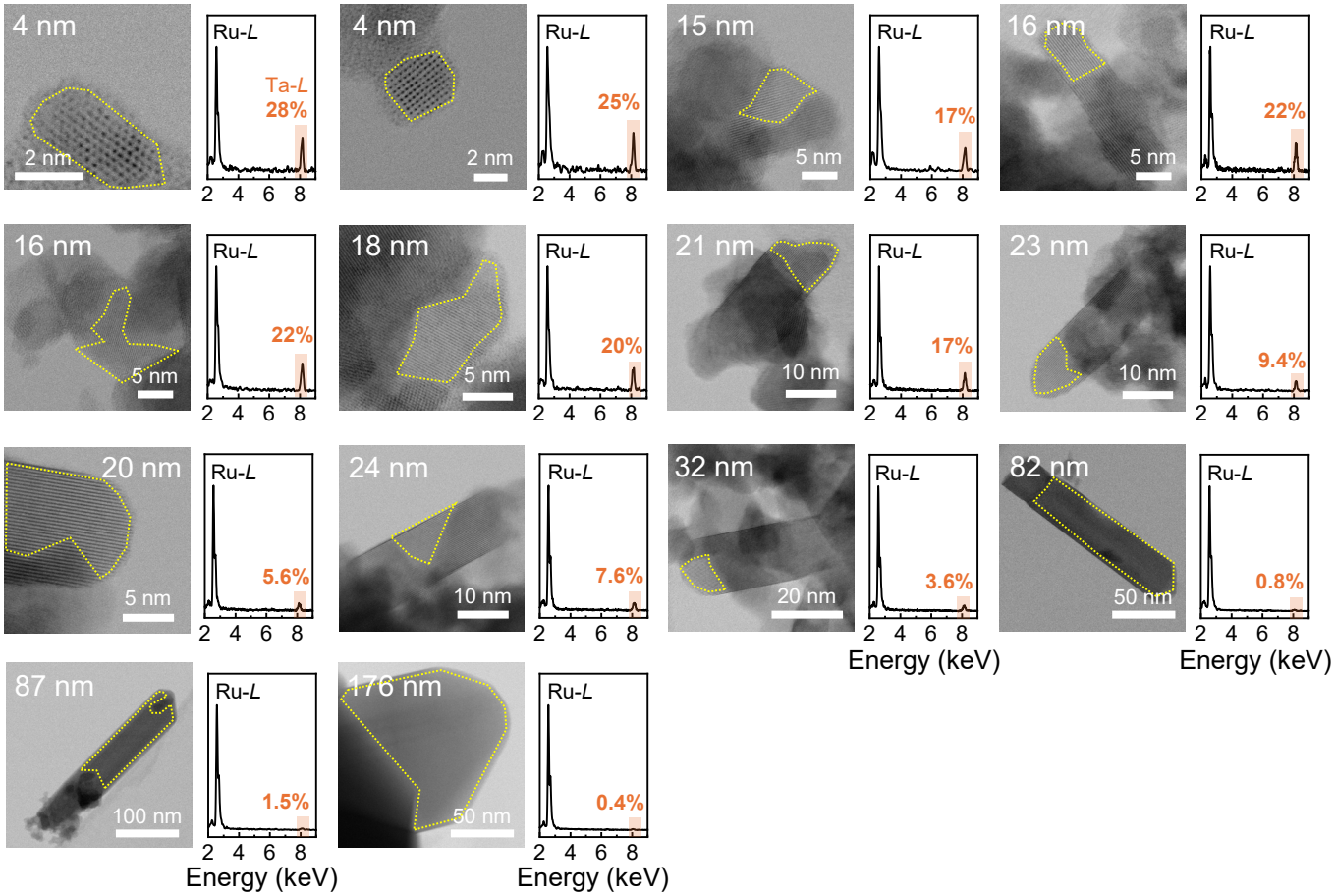

Figure S14. BF images of crystals and their EDS spectra in the sample with Ta. The images are arranged in order of increasing crystal size, as indicated within each image. Each spectrum was acquired from a single crystalline region outlined by a yellow curve. As the crystal size exceeds 20 nm, the Ta concentration drops below 10 at%. The Ta-*L* line in the spectra is highlighted with shading.

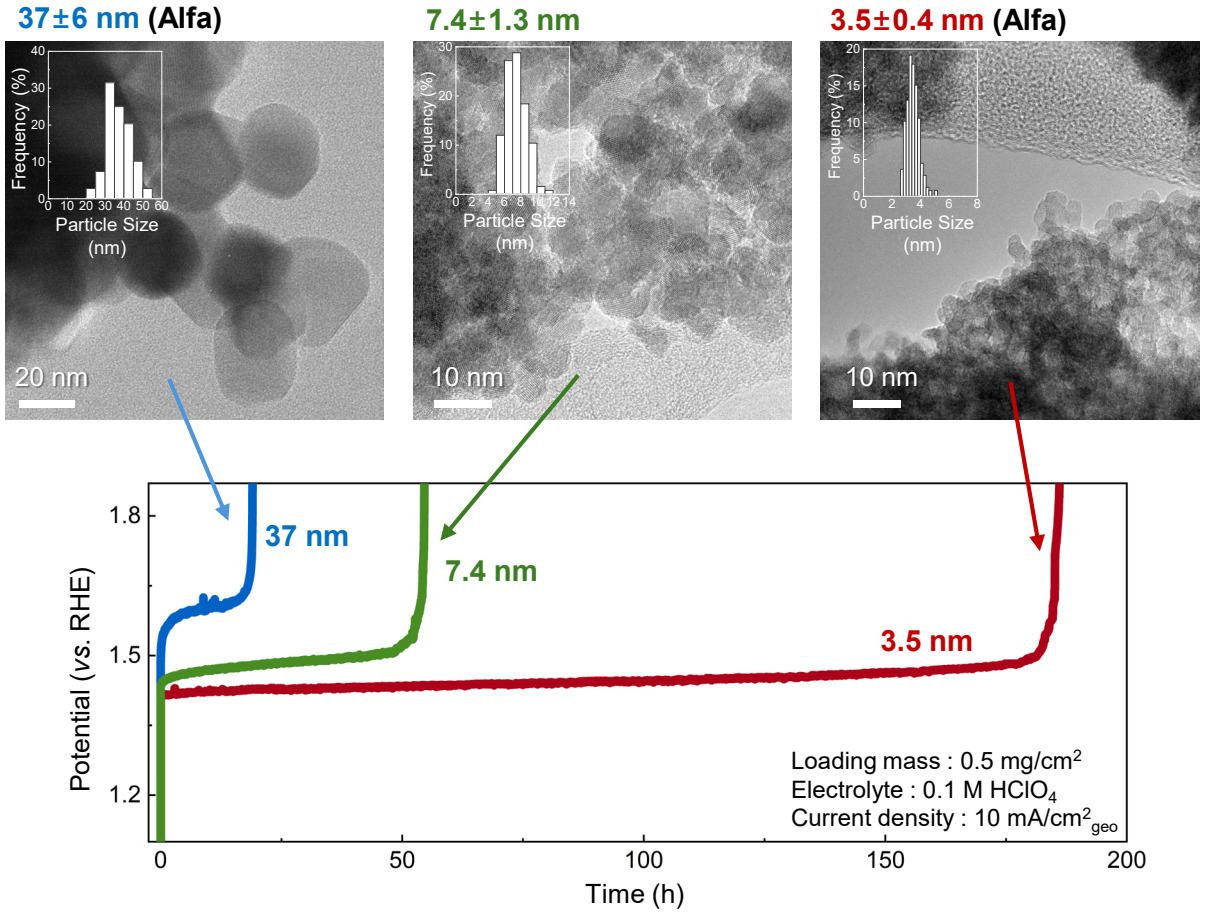

Figure S15. Chronopotentiometry (CP) tests evaluating the stability of pristine RuO_2 during the OER. As shown in the TEM images, three samples with different particle sizes were used for comparison. It is noted that the sample with the smallest particle size (3.5 nm) has the largest surface area. Consequently, 10 mA/cm^2_{geo} is achieved at the lowest overpotential among the three. Because a lower overpotential typically mitigates catalyst degradation, the sample with the smallest particles also exhibits the longest retention time (>170 h) during the CP tests. This set of experiments clearly demonstrates that the durability observed in CP-based tests is strongly influenced by the particle size of the catalysts. Owing to this pronounced particle-size dependency, CP testing is not recommended as an objective protocol for evaluating a material's intrinsic stability.

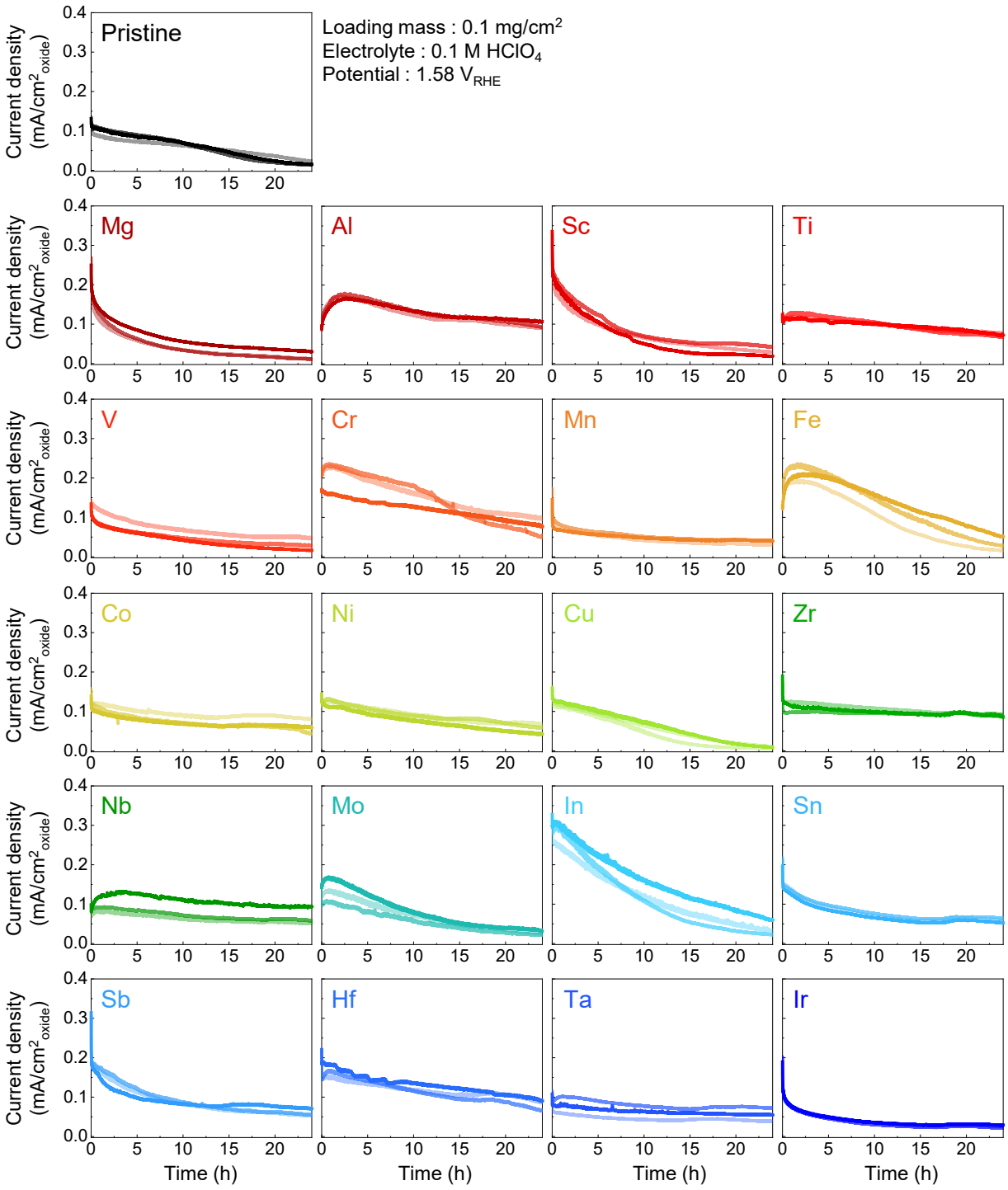

Figure S16. CA test results for solid-solution $Ru_{0.8}M_{0.2}O_2$. This set of plots shows the OER current densities measured at 1.58 V_{RHE} for 24 h for the solid-solution $Ru_{0.8}M_{0.2}O_2$ samples. Three independent specimens were tested for each foreign element to determine the corresponding S-number. A pristine RuO_2 sample was also tested for reference.

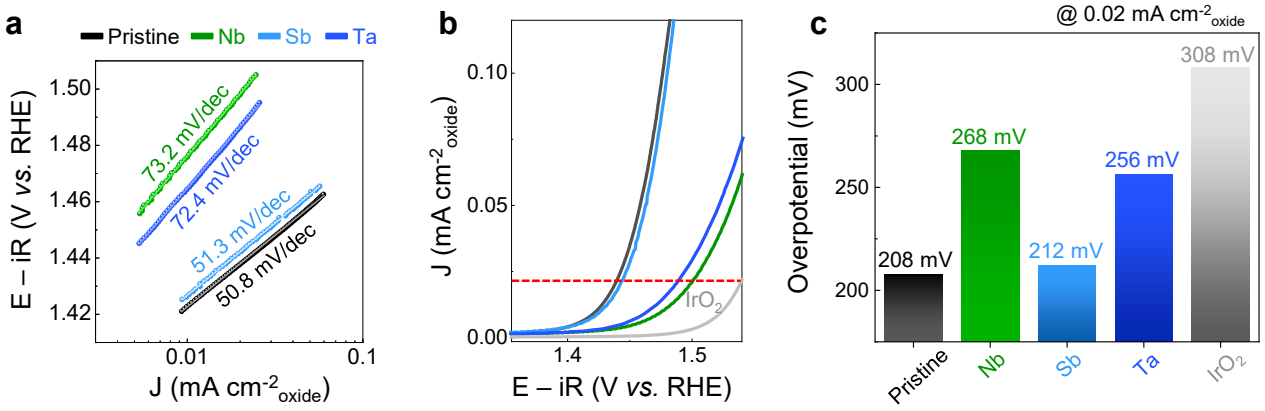

Figure S17. Catalytic activity comparison among representative stability-enhanced samples. (**a**) Tafel slope analysis shows that Nb- and Ta-doped RuO_2 exhibit reduced OER kinetics compared to the pristine and Sb-doped samples. (**b**,**c**) Linear sweep voltammetry curves further confirm that Nb or Ta doping lowers OER activity, suggesting that excessive doping with these elements should be avoided. Nevertheless, all doped samples demonstrate superior activity compared to IrO_2, indicating that they retain acceptable catalytic performance while achieving significantly enhanced stability.

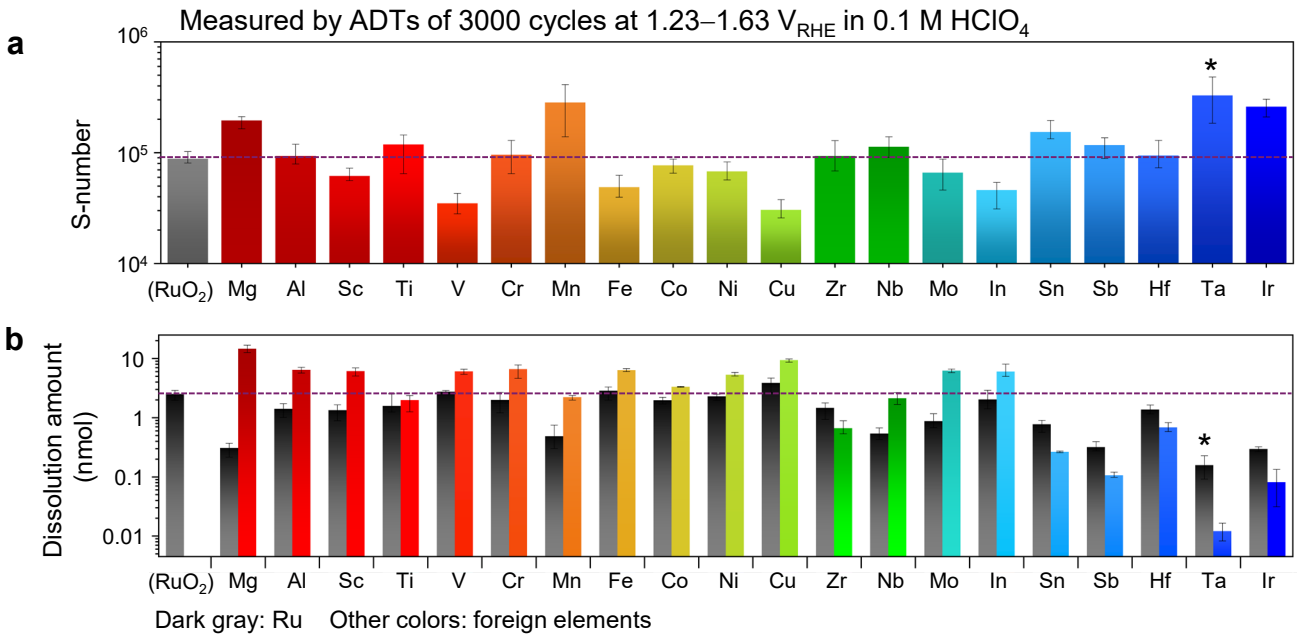

Figure S18. Additional comparison of stability among solid-solution $Ru_{0.8}M_{0.2}O_2$ electrocatalysts for the OER. For this comparison, accelerated durability tests (ADTs) were carried out over a potential range of 1.23–1.63 V_{RHE}. (**a**,**b**) Consistent with the results from the chronoamperometry (CA) tests, the solid solution containing Ta shows an exceptional S number in (a) and the lowest metal dissolution in (b), as indicated by asterisks.

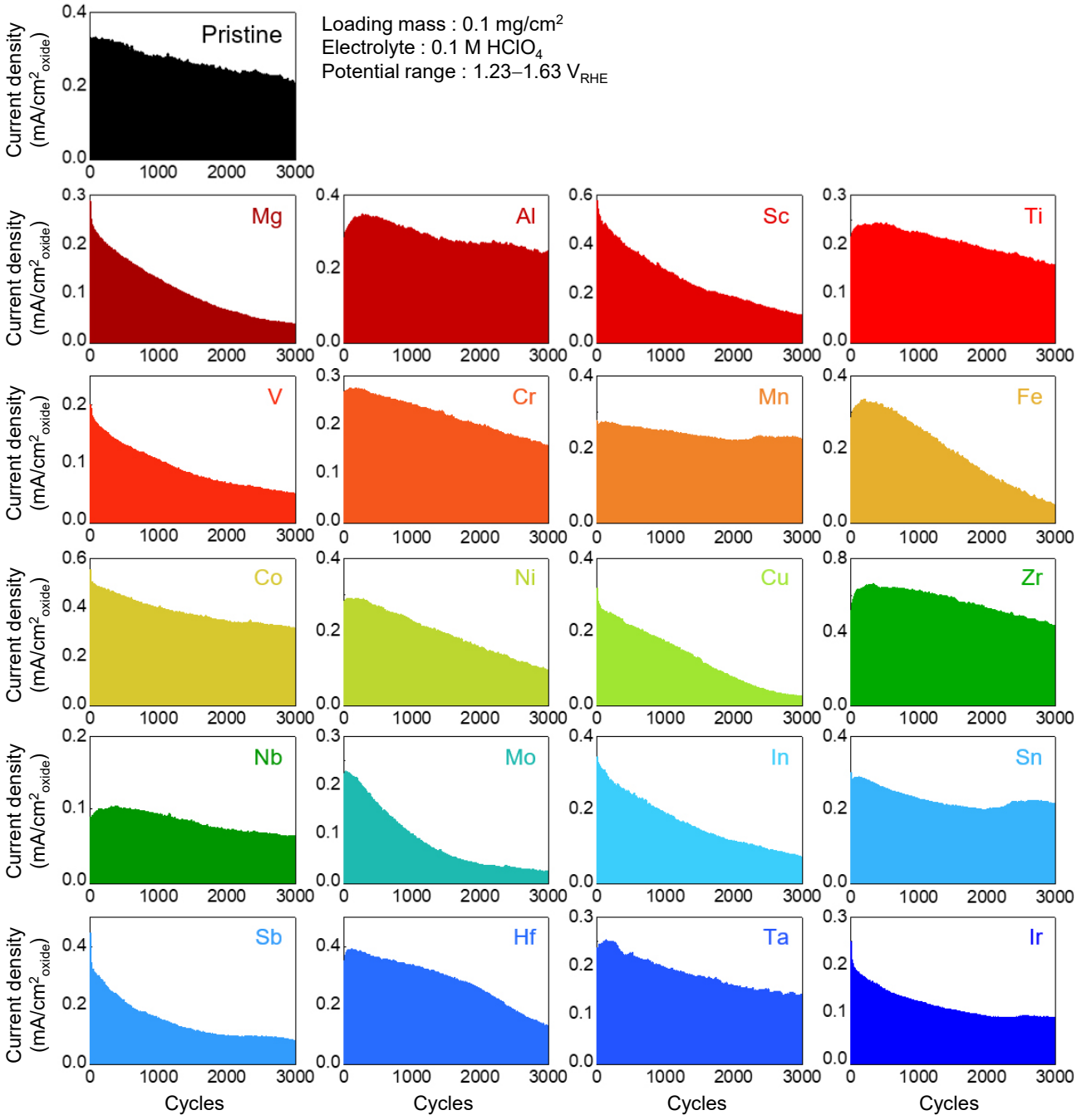

Figure S19. AST results for solid-solution $Ru_{0.8}M_{0.2}O_2$. This set of plots shows the OER current densities measured over 3000 cycles within a potential range of 1.23–1.63 V_{RHE} for the solid-solution $Ru_{0.8}M_{0.2}O_2$ samples. Three independent specimens were tested for each foreign element to determine the corresponding S-number. A pristine RuO_2 sample was also included for reference.

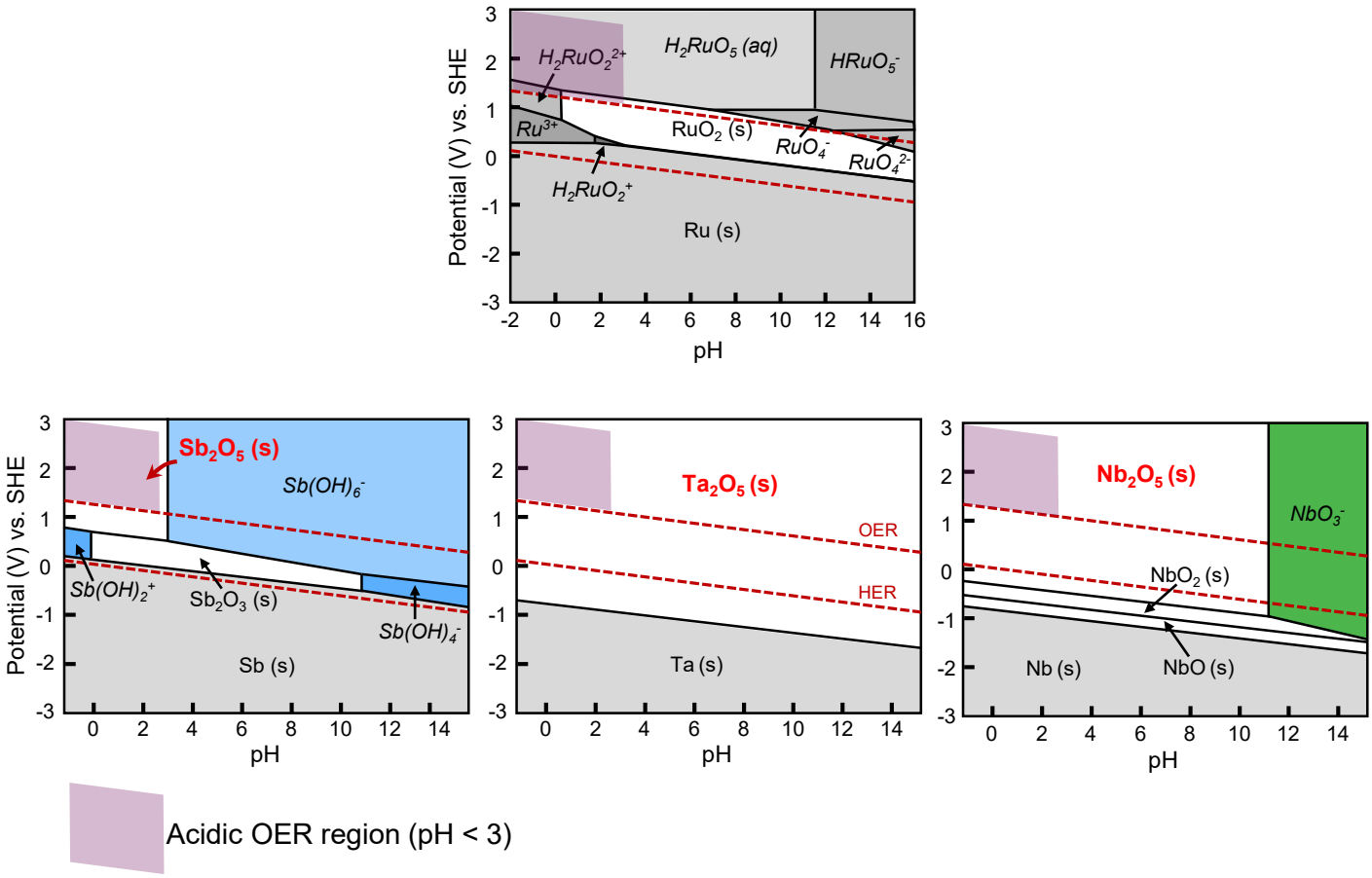

Figure S20. E–pH Pourbaix diagrams. While the electrochemically stable region of RuO_2 acidic OER conditions. This indicates high corrosion resistance of Sb, Ta, and Nb in the $Ru_{0.8}M_{0.2}O_2$ solid solutions. In particular, Ta_2O_5 shows exceptional stability across the entire pH range relevant to the OER. The Pourbaix diagram for Ru was adopted from Ref. 69, and those for Sb, Ta, and Nb from Ref. 70, as cited in the main text.

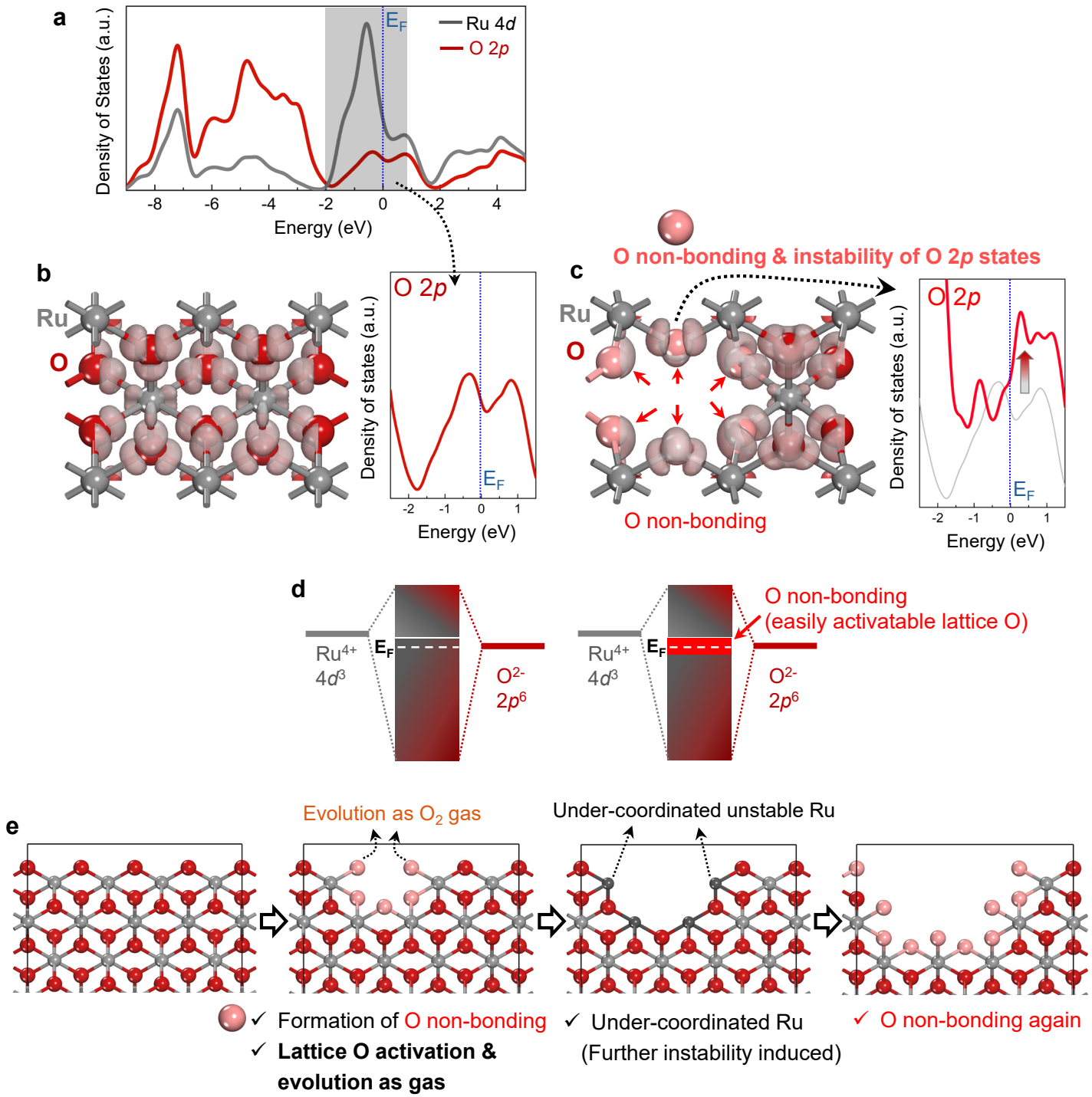

Figure S21. Ru dissolution and subsequent Ru–O instability. (**a**) The density of states (DOS) of RuO_2 is presented. A significant overlap between the Ru 4*d* and O 2*p* states is observed in the entire range below the Fermi level (E_F), indicating a high degree of covalency in the Ru–O bonding. (**b**) A magnified plot of the O 2*p* state near the E_F is shown along with an isosurface map of the electronic density difference at each atom. (**c**) Upon Ru atom dissolution and the formation of a corresponding vacancy, a non-bonding character emerges at the six surrounding O atoms, as indicated by red arrows in the electron-density isosurface map. This results in higher O 2*p* states near the E_F in the DOS plot. (**d**) The energy band diagrams describe the formation of O non-bonding states induced by Ru dissolution. Consequently, the remaining lattice O is more easily activated and can be evolve as O_2 gas under anodic potential. (**e**) A series of schematic illustrations depicts the progression of RuO_2 instability initiated by Ru dissolution. Once lattice O evolves as gas, the residual Ru cations become undercoordinated, leading to further Ru–O instability and subsequent Ru dissolution.

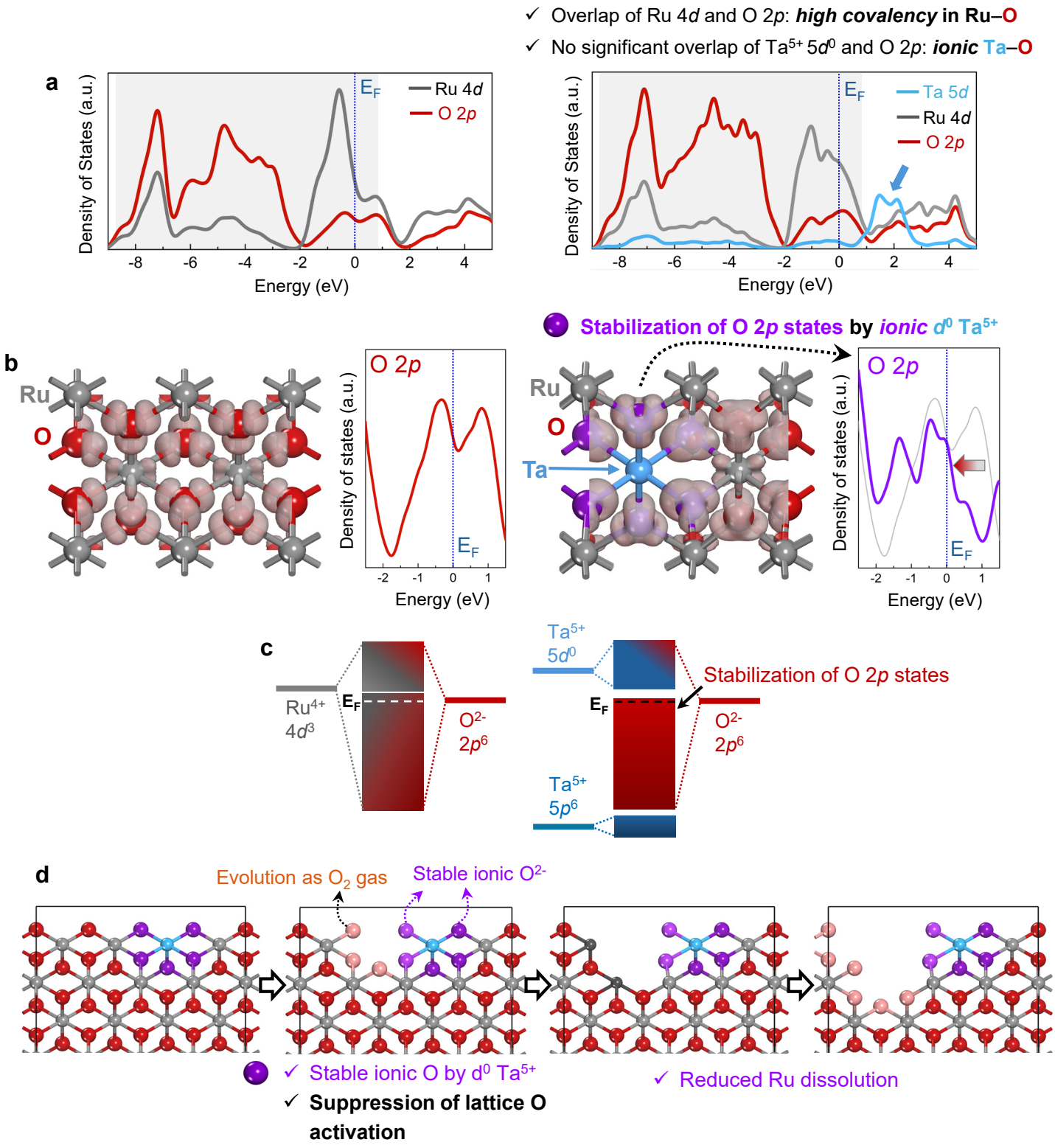

Figure S22. Role of ionic d^0 Ta^{5+} in suppressing Ru dissolution. (**a**) Plots of the DOS of pristine and Ta-doped RuO_2 show that the empty Ta $5d^0$ states predominantly lie at higher energy levels above E_F (>0.5 eV). As a result, minimal overlap occurs between the O 2*p* and Ta 5*d* states. (**b**) The fully empty d^0 configuration of ionic Ta^{5+} allows adjacent O^{2-} anions (purple) to be stabilized by achieving a fully occupied $2p^6$ configuration of O, without forming covalent bonds with Ta. The DOS plot of the six neighboring O atoms in Ta-doped RuO_2 consistently represents a substantial lowering of O 2*p* energy levels. The electronic density difference isosurface further illustrates increased electron density around O atoms adjacent to Ta. (**c**) Unlike the broad energy overlap between Ru 4*d* and O 2*p* states in pristine RuO_2 (left), Ta doping stabilizes O 2*p* states below E_F, which are separated from the unoccupied Ta 5*d* states above E_F. This electronic structure effectively suppresses electrochemical redox activation of lattice oxygen. It is thus noted that other d^0 cations, such as Ti^{4+}, Zr^{4+}, Hf^{4+}, and Nb^{5+}, will have the same effect. (**d**) A series of schematic illustrations depict how d^0 Ta^{5+} cations suppress lattice oxygen activation. The purple spheres indicate O atoms stabilized by coordination with Ta. From this perspective, Ru dissolution is mitigated; however, the catalytic activity associated with lattice oxygen activation may be reduced.

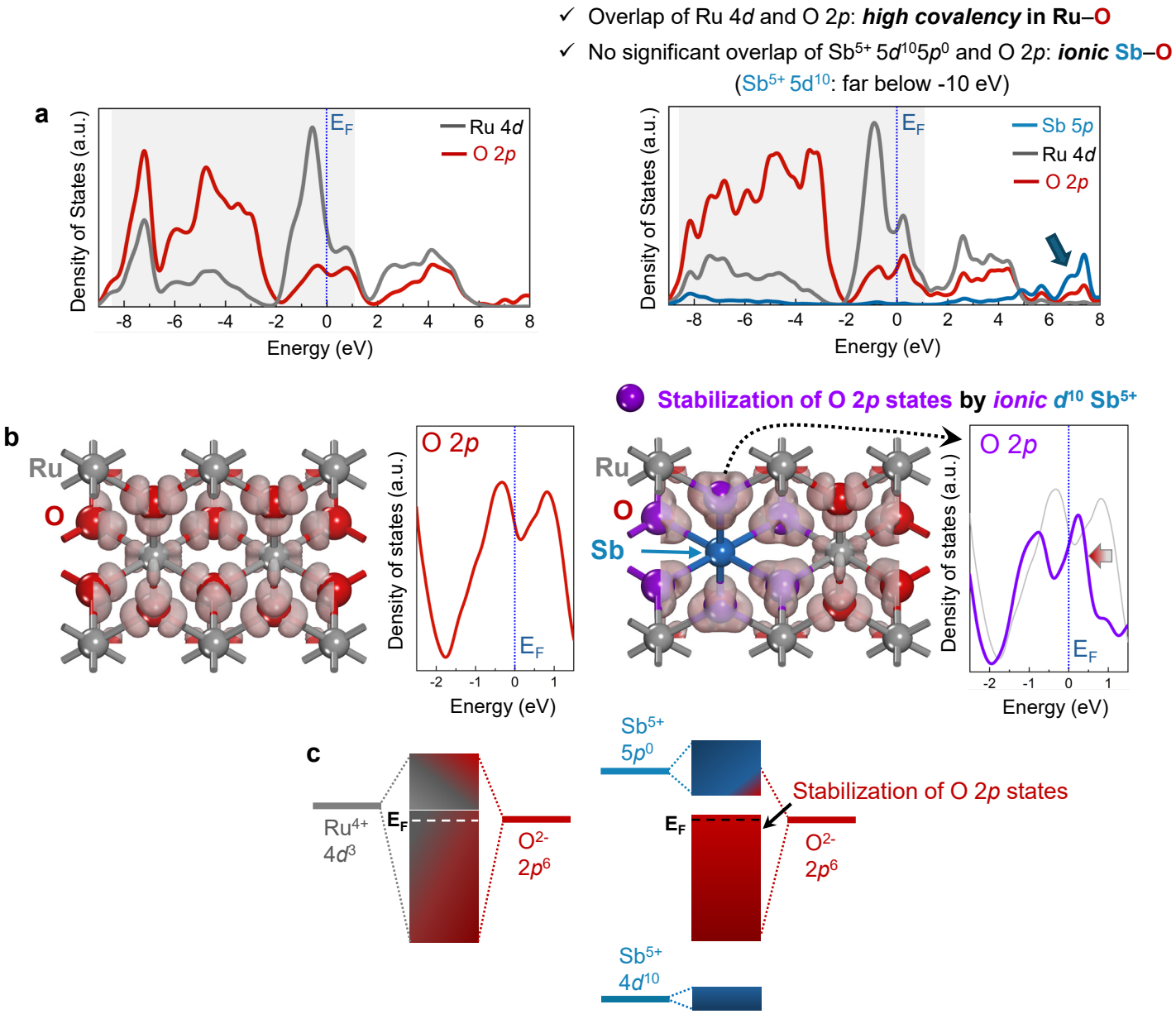

Figure S23. Role of ionic d^{10} Sb^{5+} in suppressing Ru dissolution. The effect of d^{10} Sb^{5+} is very similar to that observed in d^0 Ta^{5+}. (**a**) As demonstrated in the DOS plot of Sb-doped RuO_2, the energy level of the empty Sb^{5+} $5p^0$ states lies far above E_F, while that of the fully occupied $4d^{10}$ states is situated much further below E_F (not shown in this pot). As a result, virtually no overlap between the O 2*p* and Sb 4*d*/5*p* states is observed. (**b**) The ionic nature of Sb^{5+}, characterized by an electronic configuration of $4d^{10}$ $5s^0$ $5p^0$, stabilizes the adjacent O^{2-} anions (purple) by enabling them to achieve a fully occupied $2p^6$ configuration without forming any covalent bonds with Sb. The DOS plot of the six neighboring O atoms in Sb-doped RuO_2 (right) consistently shows noticeable energy lowering of the O 2*p* states, as indicated by an arrow. The isosurface map of the electronic density difference also demonstrates higher electron density at O atoms around Sb. (**c**) In contrast to the significant overlap between the Ru 4*d* and O 2*p* states in a very broad range of energy with no bandgap (left-hand diagram), the stabilized O 2*p* states below E_F separated from the Sb 4*d* and 5*p* states efficiently suppress the electrochemical redox activation of lattice oxygen.

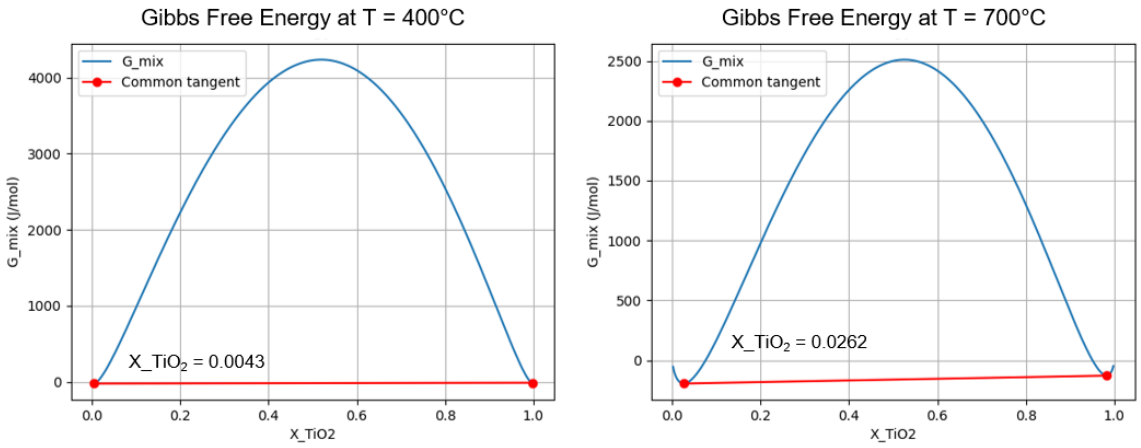

Figure S24. Binodal point estimation. The RuO_2–TiO_2 phase diagram presented in Figure 1a was adopted from Ref. 4. This set of figures illustrates how the binodal points are determined at a given temperature. The blue curves represent the Gibbs energy of mixing, while the red lines are common tangent lines, indicting the Binodal point that define the miscibility gap.

Supplementary References

S1. Halder, N. C. & Wagner, C. N. J. Separation of particle size and lattice strain in integral breadth measurements. *Acta Crystallogr*. **20**, 312–313 (1966).

S2. Merkus, H. G. *Particle Size Measurements: Fundamentals, Practice, Quality*. Ch. 2, London, Springer (2009).

S3. Zeradjanin, A. R. Frequent pitfalls in the characterization of electrodes designed for electrochemical energy conversion and storage. *ChemSusChem* **11**, 1278–1284 (2018).

S4. McCroy, C. C. L. et al. Benchmarking heterogeneous electrocatalysts for the oxygen evolution reaction. *J. Am. Chem. Soc*. **135**, 16977–16987 (2013).

S5. Geiger, S. et al. The stability number as a metric for electrocatalysts stability benchmarking. *Nat. Catal*. **1**, 508–515 (2018).

S6. Daiane Ferreira da Silva, C. et al. Oxygen evolution reaction activity and stability benchmarks for supported and unsupported IrO_x electrocatalysts. *ACS Catal*. **11**, 4107–4116 (2021).

S7. Qin, Y. et al. RuO_2 electronic structure and lattice strain dual engineering for enhanced acidic oxygen evolution reaction performance. *Nat. Commun.* **13**, 3784 (2022).

S8. Zhu, J. et al. Boosting acidic oxygen evolution electrocatalysis by engineering the interfacial water at the electrified RuO_2-electrolyte interface. *J. Am. Chem. Soc.* **147**, 47454–47466 (2025).

S9. Liu, H. et al. Grain boundary-driven synergistic dual-mechanism catalysis in RuO_2 for enhancing acidic oxygen evolution reaction activity and stability. *J. Am. Chem. Soc.* **147**, 44141–44151 (2025).

S10. Zheng, W. et al. Heteroatom dopants overcome the activity-stability trade-off in RuO_2 for acidic oxygen evolution. *Nat. Commun.* **16**, 6716 (2025).

S11. Wang, J. et al. Exceptionally active and stable RuO_2 with interstitial carbon for water oxidation in acid. *Chem* **8**, 1673-1687 (2022).

S12. Jin, M. et al. Durable acidic water oxidation ruthenium based electrocatalyst by fluorination induced symmetry breaking. *Nat. Commun.* **16**, 11615 (2025).

S13. Zhang, L. et al. Sodium-decorated amorphous/crystalline RuO_2 with rich oxygen vacancies: a robust pH-universal oxygen evolution electrocatalyst. *Angew. Chem. Int. Ed.* **60**, 18821–18829 (2021).

S14. Li, W. et al. Inhibiting overoxidation of dynamically evolved RuO_2 to achieve a win–win in activity–stability for acidic water electrolysis. *J. Am. Chem. Soc.* **147**, 10446–10458 (2025).

S15. Li, Z. et al. Mg-doping improves the performance of Ru-based electrocatalysts for the acidic oxygen evolution reaction. *Chem. Commun.* **56**, 1749–1752 (2020).

S16. Lee, K. et al. Modulating the valence electronic structure using earth-abundant aluminum for high-performance acidic oxygen evolution reaction. *Chem* **9**, 3600–3612 (2023).

S17. Liu, C. et al. Nano Si-doped ruthenium oxide particles from caged precursors for high-performance acidic oxygen evolution. *Adv. Sci.* **10**, 2207429 (2023).

S18. Ping, X. et al. Locking the lattice oxygen in RuO_2 to stabilize highly active Ru sites in acidic water oxidation. *Nat. Commun.* **15**, 2501 (2024).

S19. Jeon, D. et al. Electrochemical evolution of Ru-based polyoxometalates into Si,W-codoped RuO_x for acidic overall water splitting. *Adv. Mater.* **36**, 2304468 (2024).

S20. Hu, W. et al. Doping Ti into RuO_2 to accelerate bridged-oxygen-assisted deprotonation for acidic oxygen evolution reaction. *Adv. Mater.* **37**, 2411709 (2025).

S21. Godínez-Salomón, J. F. et al. Titanium substitution effects on the structure, activity, and stability of nanoscale ruthenium oxide oxygen evolution electrocatalysts: experimental

and computational study. *ACS Appl. Nano Mater.* **5**, 11752–11775 (2022).
S22. Wang, X. et al. Electronic structure modulation of RuO_2 by TiO_2 enriched with oxygen vacancies to boost acidic O_2 Evolution. *ACS Catal.* **12**, 9437–9445 (2022).
S23. Abed, J. et al. Pourbaix machine learning framework identifies acidic water oxidation catalysts exhibiting suppressed ruthenium dissolution. *J. Am. Chem. Soc.* **146**, 15740–15750 (2024).
S24. Qin, Q. et al. Atomically dispersed vanadium-induced Ru-V dual active sites enable exceptional performance for acidic water oxidation. *Angew. Chem. Int. Ed.* **64**, e202413657 (2025).
S25. Wu, H. et al. Engineering high-density microcrystalline boundary with V-doped RuO_2 for high-performance oxygen evolution in acid. *Nat. Commun.* **16**, 4482 (2025).
S26. Lin, Y. et al. Chromium-ruthenium oxide solid solution electrocatalyst for highly efficient oxygen evolution reaction in acidic media. *Nat. Commun.* **10**, 162 (2019).
S27. Shen, Y. et al. Cr dopant mediates hydroxyl spillover on RuO_2 for high-efficiency proton exchange membrane electrolysis. *Nat. Commun.* **15**, 7861 (2024).
S28. Zhao, X. et al. 2D ruthenium–chromium oxide with rich grain boundaries boosts acidic oxygen evolution reaction kinetics. *Small* **20**, 2311172 (2024).
S29. Chen, H. et al. Modulating the electronic structure of RuO_2 through Cr solubilizing for improved oxygen evolution reaction. *Small Methods* **6**, 2200636 (2022).
S30. Cao, X. et al. Regulation of oxide pathway mechanism for sustainable acidic water oxidation. *J. Am. Chem. Soc.* **146**, 32049–32058 (2024).
S31. Li, X. et al. Optimal selection of RuO_2 for durable oxygen evolution reactions in acidic media by continuous regulation of Ru–O covalency. *Energy Environ. Sci.* **18**, 4200–4209 (2025).
S32. Liu, Z. et al. Synergistic Sr activation and Cr buffering effect on RuO_2 electronic structures for enhancing the acidic oxygen evolution reaction. *Nano Lett.* **24**, 10899–10907 (2024).
S33. Zhang, T. et al. Atomically thin high-entropy oxides via naked metal ion self-assembly for proton exchange membrane electrolysis. *Nat. Commun.* **16**, 1037 (2025).
S34. Chen, S. et al. Mn-doped RuO_2 nanocrystals as highly active electrocatalysts for enhanced oxygen evolution in acidic media. *ACS Catal.* **10**, 1152–1160 (2020).
S35. Wang, K. et al. Highly active ruthenium sites stabilized by modulating electron-feeding for sustainable acidic oxygen-evolution electrocatalysis. *Energy Environ. Sci.* **15**, 2356–2365 (2022).
S36. Ji, Q. et al. Operando identification of the oxide path mechanism with different dual-active sites for acidic water oxidation. *Nat. Commun.* **15**, 8089 (2024).
S37. Tan, L. et al. Ferromagnetic-interaction-induced spin symmetry broken in ruthenium oxide for enhanced acidic water oxidation. *ACS Catal.* **14**, 11273–11285 (2024).
S38. Li, L. et al. Spin-polarization strategy for enhanced acidic oxygen evolution activity. *Adv. Mater.* **35**, 2302966 (2023).
S39. An, L. et al. Reconstructed $RuMnO_x$ with enhanced performance in acidic water oxidation. *Appl. Surf. Sci.* **652**, 159251 (2024).
S40. Wu, X. et al. Pluralistic electronic structure modulation of ruthenium oxide for enhanced acidic water electrolysis. *Small Struct.* **5**, 2300518 (2024).
S41. Jun, H. et al. Quantity effect of heteroatom incorporation on the oxygen evolution mechanism in ruthenium oxide. *Chem* **11**, 102367 (2025).
S42. Zhang, J. et al. Amorphous $MnRuO_x$ containing microcrystalline for enhanced acidic oxygen-evolution activity and stability. *Angew. Chem. Int. Ed.* **63**, e202405641 (2024).
S43. Xue, Z.-H. et al. Simple and scalable introduction of single-atom Mn on RuO_2 electrocatalysts for oxygen evolution reaction with long-term activity and stability. *J.*

Am. Chem. Soc. **147**, 17839–17848 (2025).
S44. Liu, Y. et al. Self-limiting surface leaching stabilizes Ru-based catalysts for acidic water oxidation. *Energy Environ. Sci.* **18**, 3352–3364 (2025).
S45. Yuan, B. et al. Synergistic niobium and manganese co-doping into RuO_2 nanocrystal enables PEM water splitting under high current. *Nat. Commun.* **16**, 4583 (2025).
S46. Xue, Y. et al. Sulfate-functionalized $RuFeO_x$ as highly efficient oxygen evolution reaction electrocatalyst in acid. *Adv. Funct. Mater.* **31**, 2101405 (2021).
S47. Tian, Y. et al. A Co-doped nanorod-like RuO_2 electrocatalyst with abundant oxygen vacancies for acidic water oxidation. *iScience* **23**, 100756 (2020).
S48. Zhu, W. et al. Direct dioxygen radical coupling driven by octahedral ruthenium–oxygen–cobalt collaborative coordination for acidic oxygen evolution reaction. *J. Am. Chem. Soc.* **145**, 17995–18006 (2023).
S49. Liu, Y. et al. Ultrathin and conformal depletion layer of core/shell heterojunction enables efficient and stable acidic water oxidation. *J. Am. Chem. Soc.* **146**, 26897–26908 (2024).
S50. Liang, J. et al. Dual-site cobalt-doped RuO_2/TiO_2 electrocatalyst enables stable and cost-efficient acidic oxygen evolution for PEM water electrolysis. *J. Am. Chem. Soc.* **147**, 39781–39795 (2025).
S51. Liu, H. et al. Cost-efficient and stable electrolysis of reverse osmosis water using a Co-RuO_2-enabled PEM electrolyser. *Nat. Catal.* https://doi.org/10.1038/s41929-025-01456-w (2026).
S52. Jin, H. et al. Safeguarding the RuO_2 phase against lattice oxygen oxidation during acidic water electrooxidation. *Energy Environ. Sci.* **15**, 1119–1130 (2022).
S53. Qian, F. et al. High-entropy RuO_2 catalyst with dual-site oxide path for durable acidic oxygen evolution reaction. *Nat. Commun.* **16**, 6894 (2025).
S54. Wu, Z.-Y. et al. Non-iridium-based electrocatalyst for durable acidic oxygen evolution reaction in proton exchange membrane water electrolysis. *Nat. Mater.* **22**, 100–108 (2023).
S55. Hao, Y. et al. Designing neighboring-site activation of single atom via tunnel ions for boosting acidic oxygen evolution. *Nat. Commun.* **15**, 8015 (2024).
S56. Su, J. et al. Assembling ultrasmall copper-doped ruthenium oxide nanocrystals into hollow porous polyhedra: highly robust electrocatalysts for oxygen evolution in acidic media. *Adv. Mater.* **30**, 1801351 (2018).
S57. Hou, L. et al. electronic and lattice engineering of ruthenium oxide towards highly active and stable water splitting. *Adv. Energy Mater.* **13**, 2300177 (2023).
S58. Zhang, D. et al. Construction of Zn-doped RuO_2 nanowires for efficient and stable water oxidation in acidic media. *Nat. Commun.* **14**, 2517 (2023).
S59. Qin, Q. et al. Tuning electronic structure of RuO_2 by single atom Zn and oxygen vacancies to boost oxygen evolution reaction in acidic medium. *J. Energy Chem.* **88**, 94–102 (2024).
S60. Sun, P. et al. Designing 3d transition metal cation-doped $MRuO_x$ as durable acidic oxygen evolution electrocatalysts for PEM water electrolyzers. *J. Am. Chem. Soc.* **146**, 15515–15524 (2024).
S61. Zhou, Y.-N. et al. Surface evolution of Zn doped-RuO_2 under different etching methods towards acidic oxygen evolution. *J. Mater. Chem. A* **10**, 16193–16203 (2022).
S62. Qin, Y. et al. Grain boundary oxygen improving the acidic oxygen evolution reaction of Zn-RuO_2@ZnO. *J. Am. Chem. Soc.* **147**, 30943–30955 (2025).
S63. Wu, L. et al. Unveiling the structure and dissociation of interfacial water on RuO_2 for efficient acidic oxygen evolution reaction. *Angew. Chem. Int. Ed.* **64**, e202413334 (2025).
S64. An, B. et al. Strontium-doped RuO_2 electrocatalyst with abundant oxygen vacancies for

boosting OER performance. *Inorg. Chem. Front.* **11**, 8935–8944 (2024).
S65. Liu, Y. et al. Effectiveness of strain and dopants on breaking the activity-stability trade-off of RuO_2 acidic oxygen evolution electrocatalysts. *Nat. Commun.* **16**, 1717 (2025).
S66. Deng, L. et al. Lewis acid-mediated interfacial water supply for sustainable proton exchange membrane water electrolysis. *J. Am. Chem. Soc.* **146**, 35438–35448 (2024).
S67. Ospina-Acevedo, F. et al. Catalytic activity and electrochemical stability of $Ru_{1-x}M_xO_2$ (M = Zr, Nb, Ta): computational and experimental study of the oxygen evolution reaction. *ACS Appl. Mater. Interfaces* **16**, 16373–16398 (2024).
S68. Liu, H. et al. Eliminating over-oxidation of ruthenium oxides by niobium for highly stable electrocatalytic oxygen evolution in acidic media. *Joule* **7**, 558–573 (2023).
S69. He, J. et al. Tuning electron correlations of RuO_2 by co-doping of Mo and Ce for boosting electrocatalytic water oxidation in acidic media. *Appl. Catal. B: Environ.* **298**, 120528 (2021).
S70. Zhang, Y. et al. Mo-doped mesoporous RuO_2 spheres as high-performance acidic oxygen evolution reaction electrocatalyst. *Small* **20**, 2305889 (2024).
S71. Gou, W. et al. Oxygen spillover from RuO_2 to MoO_3 enhances the activity and durability of RuO_2 for acidic oxygen evolution. *Energy Environ. Sci.* **17**, 6755–6765 (2024).
S72. Wang, Y. et al. Unraveling oxygen vacancy site mechanism of Rh-doped RuO_2 catalyst for long-lasting acidic water oxidation. *Nat. Commun.* **14**, 1412 (2023).
S73. Chen, S. et al. An indium-induced-synthesis $In_{0.17}Ru_{0.83}O_2$ nanoribbon as highly active electrocatalyst for oxygen evolution in acidic media at high current densities above 400 mA cm^{-2}. *J. Mater. Chem. A* **10**, 3722–3731 (2022).
S74. Wang, Y. et al. Breaking the Ru−O−Ru Symmetry of a RuO_2 Catalyst for Sustainable Acidic Water Oxidation. *Angew. Chem. Int. Ed.* **63**, e202316903 (2024).
S75. Shi, Z. et al. Customized reaction route for ruthenium oxide towards stabilized water oxidation in high-performance PEM electrolyzers. *Nat. Commun.* **14**, 843 (2023).
S76. Xu, Y. et al. Strain-modulated Ru-O covalency in Ru-Sn oxide enabling efficient and stable water oxidation in acidic solution. *Angew. Chem. Int. Ed.* **63**, e202316029 (2024).
S77. Deng, L. et al. Accelerated proton transfer in asymmetric active units for sustainable acidic oxygen evolution reaction. *J. Am. Chem. Soc.* **146**, 23146–23157 (2024).
S78. Lin, X. et al. Electronic tuning of RuO_2 polarizes metal–oxygen redox for proton exchange membrane water electrolysis. *Nat. Commun.* **16**, 8709 (2025).
S79. Xue, Y. et al. Stabilizing ruthenium dioxide with cation-anchored sulfate for durable oxygen evolution in proton-exchange membrane water electrolyzers. *Nat. Commun.* **14**, 8093 (2023).
S80. Boakye, F. O. et al. Synergistic engineering of dopant and support of Ru oxide catalyst enables ultrahigh performance for acidic oxygen evolution. *Adv. Funct. Mater.* **34**, 2408714 (2024).
S81. Song, H. et al. RuO_2–CeO_2 lattice matching strategy enables robust water oxidation electrocatalysis in acidic media via two distinct oxygen evolution mechanisms. *ACS Catal.* **14**, 3298–3307 (2024).
S82. Li, L. et al. Optimizing the electronic structure of ruthenium oxide by neodymium doping for enhanced acidic oxygen evolution catalysis. *Adv. Funct. Mater.* **33**, 2213304 (2023).
S83. Ai, B. et al. Oxygen vacancy-rich Nd-doped RuO_2 for efficient acid overall water splitting. *J. Electroanal. Chem*. **975**, 118756 (2024).
S84. Wang, C. et al. An asymmetric RE–O–Ru unit with bridged oxygen vacancies accelerates deprotonation during acidic water oxidation. *Energy Environ. Sci.* **18**, 4276–4287 (2025).
S85. Li, L. et al. Lanthanide-regulating Ru-O covalency optimizes acidic oxygen evolution

electrocatalysis. *Nat. Commun.* **15**, 4974 (2024).
S86. Wang, X. et al. RuO_2 with short-range ordered tantalum single atoms for enhanced acidic oxygen evolution reaction. *Adv. Energy Mater.* **15**, 2403388 (2025).
S87. Zhang, J. et al. Tantalum-stabilized ruthenium oxide electrocatalysts for industrial water electrolysis. *Science* **387**, 48–55 (2025).
S88. Shim, J. et al. Atomically dispersed high-valent d^0-metal breaks the activity–stability trade-off in proton exchange membrane water electrolysis. *J. Am. Chem. Soc.* **147**, 16179–16188 (2025).
S89. Natarajan, V. et al. Performance and degradation studies of RuO_2–Ta_2O_5 anode electrocatalyst for high temperature PBI based proton exchange membrane water electrolyser. *Int. J. Hydrog. Energy* **40**, 16702–16713 (2015).
S90. Bai, J. et al. Regulating Ru−O bond and oxygen vacancies of RuO_2 by Ta doping for electrocatalytic oxygen evolution in acid media. *Inorg. Chem*. **63**, 20584–20591 (2024).
S91. Hao, S. et al. Dopants fixation of ruthenium for boosting acidic oxygen evolution stability and activity. *Nat. Commun.* **11**, 5368 (2020).
S92. Wen, Y. et al. Introducing Brønsted acid sites to accelerate the bridging-oxygen-assisted deprotonation in acidic water oxidation. *Nat. Commun.* **13**, 4871 (2022).
S93. Deng, L. et al. Valence oscillation of Ru active sites for efficient and robust acidic water oxidation. *Adv. Mater.* **35**, 2305939 (2023).
S94. Wang, S. et al. Simultaneously improved activity and stability for acidic water oxidation of IrRu Oxides by a dual role of tungsten doping. *ACS Appl. Mater. Interfaces* **15**, 59432–59443 (2023).
S95. Jin, H. et al. Dynamic rhenium dopant boosts ruthenium oxide for durable oxygen evolution. *Nat. Commun.* **14**, 354 (2023).
S96. Marshall, A. T. et al. Performance of a PEM water electrolysis cell using $Ir_xRu_yTa_zO_2$ electrocatalysts for the oxygen evolution electrode. *Int. J. Hydrog. Energy* **32**, 2320–2324 (2007).
S97. Zhu, W. et al. Stable and oxidative charged Ru enhance the acidic oxygen evolution reaction activity in two-dimensional ruthenium-iridium oxide. *Nat. Commun.* **14**, 5365 (2023).
S98. Bertelsen, A. D. et al. Formation mechanism and hydrothermal synthesis of highly active $Ir_{1-x}Ru_xO_2$ nanoparticles for the oxygen evolution reaction. *J. Am. Chem. Soc.* **146**, 23729–23740 (2024).
S99. Wu, H. et al. Atomically engineered interfaces inducing bridging oxygen-mediated deprotonation for enhanced oxygen evolution in acidic conditions. *Nat. Commun.* **15**, 10315 (2024).
S100. Qiu, C. et al. Low-iridium stabilized ruthenium oxide anode catalyst for durable proton-exchange membrane water electrolysis. *Nat. Nanotechnol.* **20**, 1787–1795 (2025).
S101. Wang, J. et al. Single-site Pt-doped RuO_2 hollow nanospheres with interstitial C for high-performance acidic overall water splitting. *Sci. Adv.* **8**, eabl9271
S102. Cao, X. et al. Strain heterogeneity in RuO_2 for efficient acidic oxygen evolution reaction in proton exchange membrane water electrolysis. *Nat. Commun.* **16**, 6217 (2025).
S103. Zhou, C. et al. Pinning effect of lattice Pb suppressing lattice oxygen reactivity of Pb-RuO_2 enables stable industrial-level electrolysis. *Nat. Commun.* **15**, 9774 (2024).
S104. Yang, Z. et al. Phase-engineered Bi-RuO_2 single-atom alloy oxide boosting oxygen evolution electrocatalysis in proton exchange membrane water electrolyzer. *Adv. Mater.* **37**, 2417777 (2025).